

## DEVELOPMENTAL BIOLOGY

# Meiotic cohesin RAD21L shapes 3D genome structure and transcription in the male germline

Laia Marín-Gual<sup>1,2</sup>, Covadonga Vara<sup>1,2</sup>, Raquel Sainz-Urruela<sup>3</sup>, Yasmina Cuartero<sup>4,5</sup>,  
Lucía Álvarez-González<sup>1,2</sup>, Natalia Felipe-Medina<sup>3</sup>, Francisca García<sup>6</sup>, Elena Llano<sup>3</sup>,  
Marc A. Martí-Renom<sup>4,5,7,8</sup>, Alberto M. Pendás<sup>3\*</sup>, Aurora Ruiz-Herrera<sup>1,2\*</sup>

The distinctive three-dimensional (3D) chromatin architecture adopted by chromosomes during meiosis is essential for fertility, yet the functional implications of the fine-scale spatial organization remain poorly understood. Here, we investigate the impact of RAD21L deletion, a meiosis-specific cohesin subunit, on the 3D genome architecture and gene expression in the male germ line. Using fluorescence-activated cell sorting, high-throughput chromosome conformation capture, and single-cell RNA sequencing, we demonstrate that RAD21L deficiency impairs meiotic chromatin organization and inter/intrachromosomal interactions. This conspicuous 3D genome reorganization also disrupts bouquet formation, resulting in increased telomeric interactions between heterologous chromosomes in primary spermatocytes. Genome reorganization was accompanied by detectable transcriptional dysregulation in spermatogonia and primary spermatocytes, mainly affecting sex chromosomes. Collectively, our findings establish the cohesin RAD21L as a germline-specific critical regulator of genome-wide 3D genome reorganization during spermatogenesis and a modulator of the male germline transcriptional landscape.

## INTRODUCTION

The hierarchical organization of the genome undergoes dramatic changes during gametogenesis (1–4). However, how loop-extruding factors such as meiotic cohesins fine-tune chromatin reorganization in coordination with transcription remains largely unknown. Elucidating the spatiotemporal dynamics of higher-order chromatin architecture during gametogenesis is key to understanding the mechanisms underpinning fertility and their impact on genetic diversity, with long-term implications for genome function and evolution (5–7).

Meiosis entry is accompanied by fundamental changes in chromosome nuclear distribution, DNA methylation, histone modifications, and transcription (1, 8, 9). As meiosis progresses, both A/B compartments and topologically associated domains (TADs) attenuate to accommodate major events that take place during prophase I, including chromosomal movements, DNA scaffold assembly in the form of the synaptonemal complex, and the formation and repair of DNA double-strand breaks (DSBs) (1–4). Later, compartments and chromosomal territories reappear in postmeiotic cells (round spermatids and sperm), although both types of haploid cells adopt a distinctive chromatin structure to allow histone-to-protamine transition and cellular differentiation (1, 10).

Meiotic cohesin subunits (i.e., REC8, RAD21L, STAG3, or SMC1 $\beta$ ) play a critical role in chromosome architecture during prophase I (11–13). They are required for chromosome synapsis between

homologs, as they are involved in the formation of the chromosomal axis, holding chromatin loops to the axes and determining the number and location of DNA loops (13–15). Both RAD21L and REC8 are localized at the connection sites between lateral elements (LEs) and transverse filaments of the synaptonemal complex in pachynema, with RAD21L locating interior to REC8 sites (16). Whereas RAD21L is involved in tethering homologous chromosomes, REC8 is preferentially involved in sister chromatid cohesion (17). RAD21L is essential for spermatogenesis, as deficient mice are infertile and show impaired synapsis of homologous chromosomes, fragmented LEs with aberrant synapsis, and defective DSB processing, resulting in an accumulation of unrepaired DSBs in early stages of meiosis (11). Likewise, the attachment of telomeres to the nuclear envelope during meiosis is partially misregulated, highlighting the role of cohesins in telomere homeostasis (18, 19).

Meiotic cohesins are loaded at active promoters in both primary spermatocytes and round spermatids (1), hinting at a functional role beyond their established contribution to meiotic chromosome axis formation (11). The correlation between cohesin occupancy and the expression of genes implicated in early embryonic development suggests that cohesins could have a synergistic role in establishing transcriptional hubs during prophase I and fine-tuning subsequent spermatogenesis (1). Previous studies in somatic cells have shown that cohesin deletion prevents activation of inducible genes (20), supporting the role of cohesins in shaping lineage-specific gene regulation (21). This has been associated with extensive rewiring of promoter contacts (22). Whether this pattern applies for germ cells is currently unknown.

Here, we investigate the impact of RAD21L deletion on three-dimensional (3D) genome architecture and transcription in the mouse male germ line by integrating fluorescence-activated cell sorting (FACS), genome-wide high-throughput chromosome conformation capture analysis (Hi-C), and single-cell RNA sequencing (RNA-seq). We demonstrate that loss of RAD21L disrupts proper chromatin condensation during meiosis, leading to altered genome compartmentalization and changes in the balance of inter- and intrachromosomal

<sup>1</sup>Departament de Biologia Cel·lular, Fisiologia i Immunologia, Universitat Autònoma de Barcelona, Cerdanyola del Vallès, Spain. <sup>2</sup>Genome Integrity and Instability Group, Institut de Biotecnologia i Biomedicina, Universitat Autònoma de Barcelona, Cerdanyola del Vallès, Spain. <sup>3</sup>Molecular Mechanisms Program, Centro de Investigación del Cáncer and Instituto de Biología Molecular y Celular del Cáncer (CSIC-Universidad de Salamanca), Salamanca, Spain. <sup>4</sup>CNAG, Centre Nacional d'Anàlisi Genòmic, Barcelona, Spain. <sup>5</sup>Centre for Genomic Regulation, The Barcelona Institute for Science and Technology, Barcelona, Spain. <sup>6</sup>Unitat de Cultius Cel·lulars, Universitat Autònoma de Barcelona, Cerdanyola del Vallès, Spain. <sup>7</sup>Pompeu Fabra University, Barcelona, Spain. <sup>8</sup>ICREA, Barcelona, Spain.

\*Corresponding author. Email: aurora.ruizherrera@uab.cat (A.R.-H.); amp@usal.es (A.M.P.)

interactions in both premeiotic (spermatogonia) and meiotic (primary spermatocytes) cells. In addition, we observe defects in bouquet formation, characterized by increased telomeric interactions between heterologous chromosomes in primary spermatocytes. Moreover, this genome reorganization is accompanied by transcriptional dysregulation, detectable from the spermatogonia stage onward. Our findings establish a dual role for RAD21L in gene regulation and chromatin reorganization during early meiosis, providing direct evidence of its function in transcriptional control in both spermatogonia and primary spermatocytes.

## RESULTS

### Deletion of RAD21L-containing cohesin complexes reshapes chromatin reorganization in premeiotic and meiotic cells

We analyzed the effects of cohesin deletion in chromatin architecture during mammalian spermatogenesis using mice deficient in one of the meiosis-specific kleisins, RAD21L [hereafter RAD21L knockout (KO)] (11, 12). Highly enriched premeiotic (spermatogonia) and primary spermatocytes at the leptotene/zygotene (L/Z) stage were isolated by FACS (Fig. 1A and fig. S1). For each germ cell fraction (spermatogonia and primary spermatocytes in the L/Z stage), we performed in situ Hi-C (Fig. 1B). As KO mice are infertile due to meiotic arrest (11), advanced meiotic stages (pachytene/diplotene stages or round spermatids) were absent. For comparison, somatic Hi-C data was generated from primary cultured embryonic fibroblasts from a male RAD21L KO mouse (see Materials and Methods), while wild-type (WT) somatic and germ cell Hi-C data were obtained from previously published datasets (1), consistent with previous descriptions in both adult (3, 4, 10) and juvenile (23) mice. After filtering, we obtained an average of 235.08 million valid reads per germ cell type (tables S1 and S2), with high correlation values (from 0.94 to 0.98) between biological replicates (fig. S1).

As expected for a meiotic-specific cohesin subunit, RAD21L deficiency did not affect higher-order chromatin features in somatic cells, as exemplified in the genome-wide interaction maps, distance-dependent interaction frequency, and inter/intrachromosomal interaction ratio plots in fibroblasts (Fig. 1, B to E). In contrast, differences emerged in the germline, detecting different patterns of chromosome nuclear disposition and inter/intrachromosomal interaction ratios between genotypes (WT and KO). This was already evident in spermatogonia with further changes in primary spermatocytes (L/Z), suggesting a role of RAD21L in early compaction of chromosomes even before meiosis entry (attending the observed changes in spermatogonia) (Fig. 1, C and D).

Specifically, spermatogonia from KO mice showed increased mean levels of inter/intrachromosomal interaction ratios ( $0.80 \pm 0.10$ ) when compared to WT spermatogonia ( $0.33 \pm 0.05$ ), resembling the somatic-like pattern observed in fibroblasts ( $0.78 \pm 0.09$ ) (Fig. 1C). This trend was also evident in heatmaps of genome-wide interchromosomal interactions (Fig. 1D). However, contact probability curves and estimated DNA loop sizes in spermatogonia showed only subtle or no differences between genotypes (Fig. 1, E and F), suggesting that RAD21L, although expressed at low levels, may already influence chromatin organization at this stage (i.e., relaxation of chromatin compaction exemplified as an increase in interchromosomal interactions and a reduction in intrachromosomal interactions) and interdigitation between chromosomes. Supporting this, a close inspection of published bulk RNA-seq data (1) confirmed the presence of

RAD21L transcripts already in spermatogonia, along with other meiotic cohesins (fig. S2), mirroring previous reports (24–27).

As meiosis progressed, further architectural differences became apparent in early primary spermatocytes (L/Z). In KO mice, there was an increase in interchromosomal interactions when compared to WT mice, which was translated into higher mean rates of inter/intrachromosomal interaction ratios ( $0.56 \pm 0.05$ ) when compared to WT ( $0.23 \pm 0.01$ ) (Fig. 1, C and D, and fig. S3, A and B), resembling a spermatogonia-like pattern (fig. S1D). Differences were also detected when analyzing distance-dependent interaction frequencies, revealing a distinct chromosome organization for primary spermatocytes, with two abrupt changes in slope: the first at 0.2 megabase pairs (Mbp) and the second at 10 Mbp (Fig. 1E). The average DNA loop size, estimated as the peak of the slope (derivative) of the  $P(s)$  function (28), indicated reduced chromatin compaction in RAD21L-deficient primary spermatocytes, with loop sizes averaging 850 kb in KO versus 650 kb in WT (Fig. 1F).

Together, these observations indicate that RAD21L deletion induces notable structural reorganization of the genome in both spermatogonia and primary spermatocytes, resulting in dynamic alterations in chromosome occupancy and folding.

### RAD21L counteracts nuclear compartmentalization in prophase I

Compartmentalization was also affected by RAD21L deletion (Fig. 2 and fig. S3). While no significant changes in A/B compartments were detected in fibroblasts and spermatogonia, marked differences between genotypes emerged in primary spermatocytes (Fig. 2, A and B, and fig. S3, C to F). Although A/B compartments are known to attenuate from the leptotene to the diplotene stage in both adult (1, 3, 4, 10) and juvenile (23) mice, primary spermatocytes from KO mice showed a more pronounced compartmentalization, with the plaid pattern persisting during meiosis (Fig. 2, A and B). Notably, A/B compartments in KO spermatocytes highly correlated with those in spermatogonia ( $r^2 = 0.94$ ) (Fig. 2B), indicating that RAD21L is a key determinant of compartment-level chromatin structure in germ cells. Given that KO mice display fragmented LEs with aberrant synapsis cytologically (11), it is plausible that the chromatin not correctly assembled into chromosomal axes retains a spermatogonia-like compartmentalization.

### Rad21l deletion increases telomeric heterologous interactions in prophase I and impairs bouquet formation

Given prior cytological evidence of abnormal telomere attachment to the nuclear envelope in RAD21L-deficient spermatocytes (11, 12), we examined this phenomenon more into detail. One structural feature characteristic of early meiosis is bouquet formation (29, 30), which is illustrated as an “X-shape” in the interchromosomal Hi-C heatmaps in primary spermatocytes (1, 3, 4) (Fig. 2C). Our analysis revealed that in RAD21L-deficient primary spermatocytes, telomeres do not cluster in the so-called bouquet but form aberrant interactions between heterologous telomeres. This was exemplified by the loss of the X-shape in the interchromosomal interaction maps (Fig. 2C) and the presence of an increase in telomere interactions between heterologous chromosomes (Mann-Whitney test,  $P < 0.05$ ) (Fig. 2, C to G). Notably, the increase in telomere interactions was only detected between chromosomal ends of q-arms (Fig. 2F), but not between chromosomal ends of p-arms, where centromeres are located (Mann-Whitney test,  $P > 0.05$ ) (Fig. 2E).

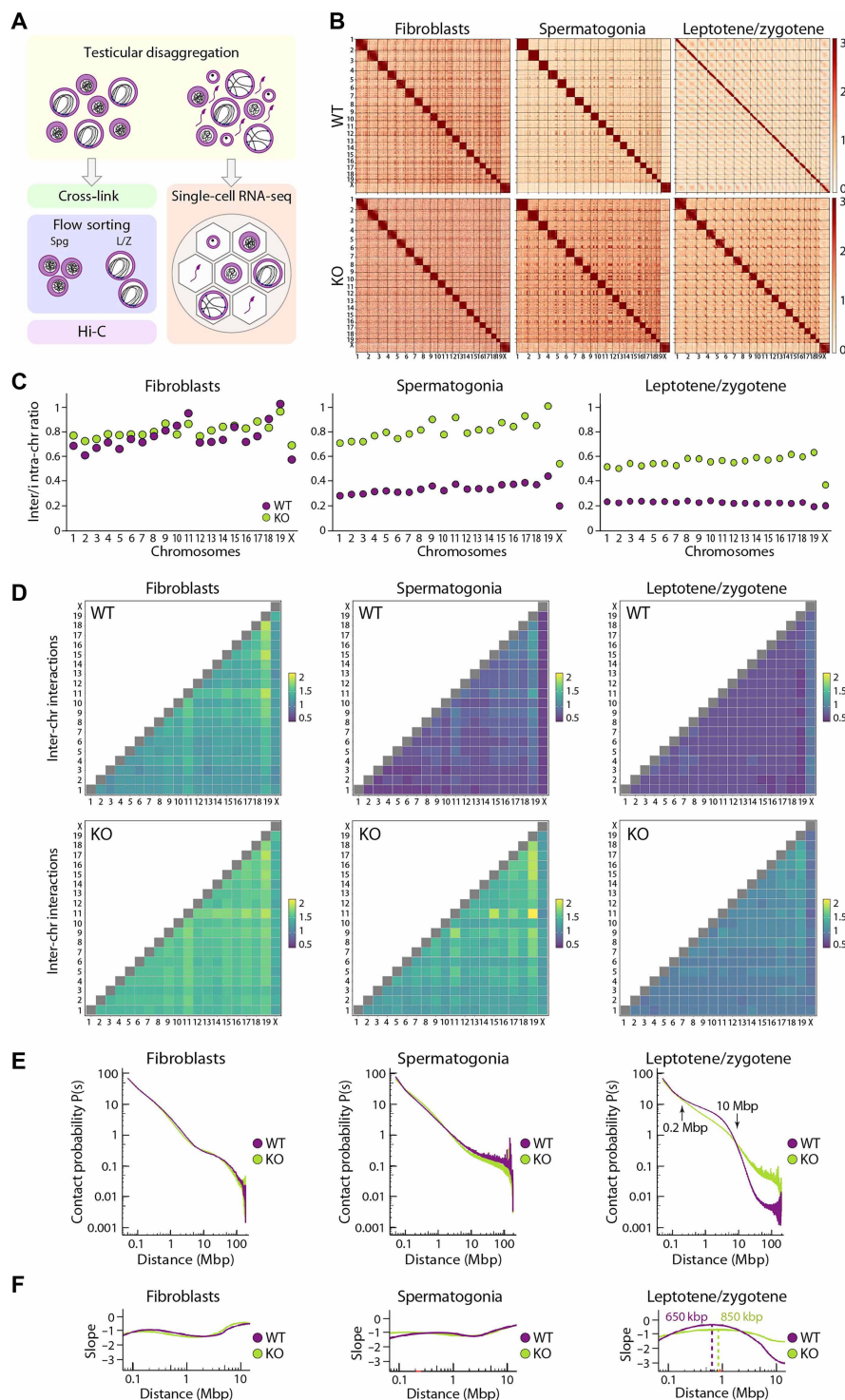


**Fig. 1. Higher-order chromatin structure.** (A) Schematic of the experimental workflow. Spg, spermatogonia. (B) Genome-wide ICE (iterative correction and eigenvector decomposition)-corrected Hi-C heatmaps at 500 kilo-base pairs (kbp) for the three cell types and genotypes analyzed. (C) Inter- and intra-chromosomal (chr) interaction ratios for each chromosome, stratified by cell types and genotypes. (D) Heatmaps depicting genome-wide interchromosomal interactions in WT (*Rad21*<sup>+/+</sup>) and KO (*Rad21*<sup>-/-</sup>) mice. Chromosomes in yellow-green indicate higher interactions frequencies, while those in dark blue indicate lower frequencies. (E) Genome-wide contact probability  $P(s)$  as a function of genomic distance for all cell types and genotypes analyzed. Arrows indicate changes in slope between genotypes. (F) Slope of the genome-wide contact probability  $P(s)$  along genomic distance. Dashed vertical lines indicate estimated DNA loop size.



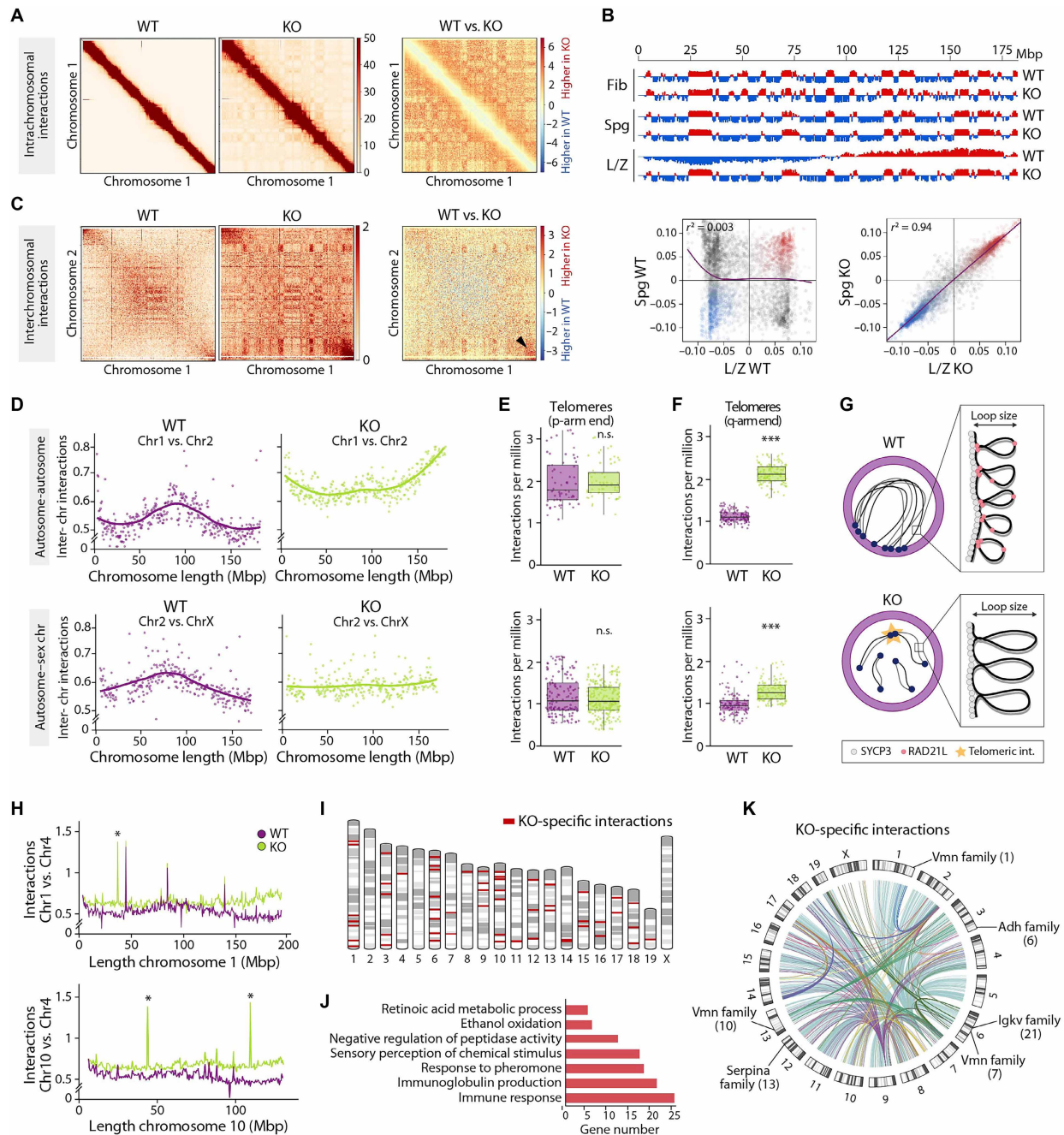


**Fig. 2. Changes in chromosomal compartmentalization and heterologous interactions.** (A) Chromosome-specific Hi-C matrices in the L/Z stage and the corresponding differential matrix. Red and blue indicate increased interactions in KO and WT mice, respectively. This pattern is consistent across all autosomes. (B) Top: Compartment signal (first eigenvector) along chromosome 2 for all cell types and genotypes. Bottom: Genome-wide correlation of first eigenvector values between spermatogonia and L/Z for both genotypes. Each dot represents a 500-kbp bin, with conserved A compartments in red, conserved B compartments in blue, and bins with ambiguous or switching compartment in gray. The coefficient of determination ( $r^2$ ) is represented for each pairwise comparison. Fib, fibroblasts. (C) Hi-C heatmaps showing interchromosomal interactions in the L/Z stage and the corresponding differential matrix. Red and blue indicate increased interactions in KO and WT mice, respectively. The observed pattern is consistent across all autosomes. (D) Representation of interchromosomal interactions along chromosomal length as smooth lines between autosomes (top) and between autosomes and the X chromosome (bottom) in the L/Z stage. The autosome-autosome interaction pattern is consistent across all autosomes. (E) Representation of telomeric interactions between p-arm ends of autosomes (top) and autosome-X chromosome pairs (bottom) in the L/Z stage. Mann-Whitney test [nonsignificant (n.s.),  $P > 0.05$ ]. (F) Representation of telomeric interactions between q-arm ends of autosomes (top) and autosome-X chromosome pairs (bottom) in the L/Z stage. Mann-Whitney test ( $***P < 0.001$ ). (G) Schematic model illustrating aberrant chromosome reorganization in the absence of RAD21L. (H) Representation of interchromosomal interactions along chromosomal length in the L/Z stage. Asterisks denote KO-specific LRLs. (I) Mouse ideogram highlighting KO-specific LRLs in red. (J) Gene Ontology (GO) analysis of genes located in the KO-specific LRLs. (K) Circos plot representing KO-specific LRLs across the mouse genome, with gene families enriched in these regions. The number of genes enriched in each region is shown in parenthesis. Vmn, vomeronasal receptor; Adh, alcohol dehydrogenases; Igkv, immunoglobulin kappa variable.

Telomere clustering into the bouquet facilitates homolog alignment and pairing via cytoplasmic microtubule movements (29, 31). Our results indicate that RAD21L deficiency disrupts bouquet formation and/or exit. Specifically, we identified 55 long-range aberrant heterologous interactions (LRIs) that were KO specific (Fig. 2H and table S3), involving all chromosomes except chromosomes 2, 5, and the X (Fig. 2, I and K). Detailed analysis of these LRIs revealed enrichment ( $P < 0.05$ ) for genes associated with the immune system (25 genes), peptidase activity (12 genes), and sensory perception of chemical stimulus (17 genes), including vomeronasal and olfactory receptors (Fig. 2, J and K, and table S4).

### **RAD21L deletion is associated with TAD reorganization in both premeiotic and meiotic cells**

To further investigate higher-order chromatin dynamics at the sub-megabase scale, we identified TADs and examined boundary robustness using TADbit (32) at a resolution of 500 kilo-base pairs (kbp) (Fig. 3A). To quantify boundary strength, we calculated the insulator score for each TAD boundary using FAN-C (33). With this metric, more negative insulator score values indicate stronger TAD boundaries, whereas values approaching zero reflect weaker or less defined boundaries (Fig. 3B).

TADs were well defined in fibroblasts and spermatogonia with differences between genotypes depending on the cell type. As expected, we did not detect major changes in fibroblasts, where TADs were detected with similar insulation scores between WT and KO fibroblasts (Mann-Whitney test,  $P = 0.89$ ) and a high percentage of

TAD boundaries (65.8%; 417 conserved TAD boundaries from a total of 634 in WT mice) was conserved between genotypes (Fig. 3, A and B, and fig. S3, G and H). In spermatogonia, we also detected a high percentage of conserved TAD boundaries (60.3%; 219 conserved TAD boundaries from a total of 363 in WT mice) (Fig. 3A). However, TADs in KO spermatogonia had a statistically significant higher TAD boundary strength than WT mice (Mann-Whitney test,  $P < 0.001$ ) (Fig. 3B and fig. S3H), as depicted in the metaborder plots (fig. S3G).

In primary spermatocytes, TAD boundary strength was reduced in both WT and KO mice compared to earlier stages (i.e., spermatogonia) (Fig. 3B and fig. S3, G and H). Despite this global attenuation in TAD insulation, only a small proportion of TAD boundaries (32.4%; 95 conserved TAD boundaries from a total of 293 in WT mice) were conserved in KO mice relative to WT (Fig. 3A). Thus, the transition from spermatogonia to primary spermatocytes is characterized by a substantial loss of TAD insulation in both genotypes, consistent with prior reports in adult (1, 3, 4) and juvenile (23) mice. KO mice retained slightly higher TAD boundary strength than WT in both spermatogonia and primary spermatocytes (Mann-Whitney test,  $P < 0.001$ ), suggesting that RAD21L ablation may delay or impair the normal attenuation of TAD insulation during meiotic progression (Fig. 3B and fig. S3H).

To explore the molecular basis of these changes, we performed a multiassociation analysis comparing conserved and altered TAD boundaries in WT and KO primary spermatocytes with RAD21L-binding sites (see Materials and Methods). We found a positive

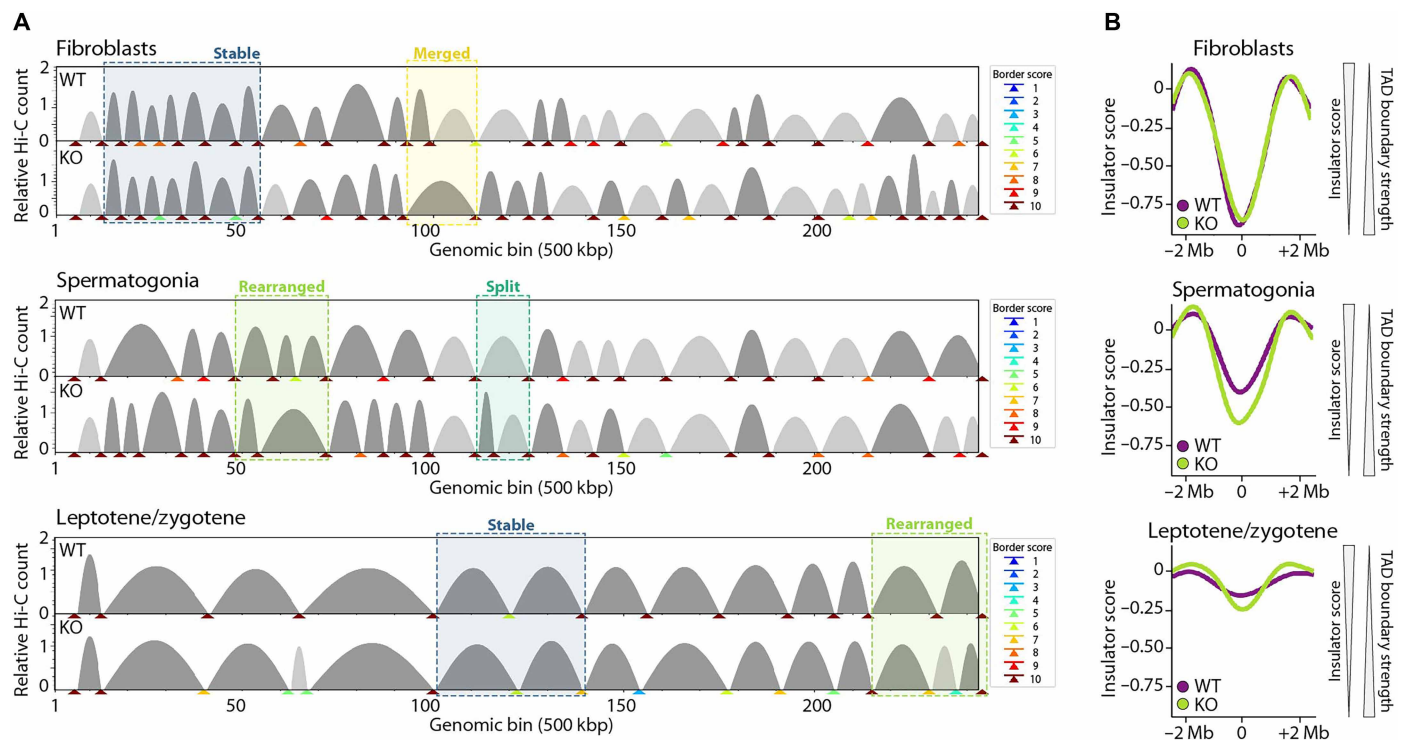


**Fig. 3. Variation at the fine scale.** (A) Representative alignments of TAD boundaries along chromosome 11 of fibroblasts, spermatogonia, and L/Z stage cells from WT and KO mice. Examples of stable, split, rearranged, and merged TADs are indicated. TAD boundary scores are also shown, reflecting the strength of each TAD boundary. (B) Insulation score profile at TAD boundaries in fibroblasts, spermatogonia, and L/Z stage spermatocytes from WT and KO mice. To the right of each panel, a schematic interpretation of insulation scores is provided: Lower and more negative values correspond to stronger TAD boundaries, while values approaching zero indicate weaker boundary strength.

association between altered TAD boundaries and the presence of RAD21L, whereas conserved boundaries did not show this enrichment (fig. S3I). These findings suggest that RAD21L contributes to the dynamic regulation of TAD architecture during the transition from premeiotic to meiotic stages, potentially by mediating cohesin replacement at specific genomic loci.

### RAD21L deficiency alters transcriptional landscapes of key meiotic genes

To assess the impact of RAD21L deletion on gene expression at single-cell resolution, we performed single-cell RNA-seq analysis using the 10x Genomics platform on whole testes from WT and KO mice at postnatal day 55 (see Materials and Methods). After quality filtering, we retained a total of 5250 WT and 6248 KO single cells for downstream analyses. Annotation of cell types was performed as previously described (34) (see Materials and Methods, Fig. 4, and fig. S4), based on expression levels of known marker genes (fig. S5), and visualized using dimensionality reduction techniques. All expected germ cell populations were identified in WT mice, including spermatogonia, primary spermatocytes (early prophase 1/2, mid-prophase, late prophase 1/2, diplotene, metaphase I, and metaphase II), round spermatids (from S1 to S7), and elongating spermatids (from S8 to S11) (Fig. 4A). In contrast and consistent with an early meiotic arrest in KO mice (11, 12), cells corresponding to later stages of prophase I and spermiogenesis were undetected in KO samples (Fig. 4, B and C, and fig. S4).

To further resolve the heterogeneity of early germ cell populations, we performed iterative clustering and annotation, identifying three spermatogonial subtypes: undifferentiated (e.g., *Sox4* and *Tubb5*), differentiated spermatogonia 1 (*Stra8* and *Uchl1*), and differentiated spermatogonia 2 (*Ccnd1* and *Esx1*). We further delineated four primary spermatocyte subtypes: leptotene (*Prdm9* and *Smc1b*), zygotene (*Sycp3* and *Sycp1*), pachytene 1 (*Hormad1* and *Piwil2*), and pachytene 2 (*Spata16* and *Spink2*) (Fig. 4D and figs. S4B and S5C). Subtype classification was guided by conserved stage-specific gene markers (34) and validated through comparative analysis (see Materials and Methods).

In KO mice, transcriptional profiles were predominantly restricted to spermatogonial subtypes (undifferentiated spermatogonia, differentiated spermatogonia 1, and differentiated spermatogonia 2) and early primary spermatocytes (L/Z stages). Notably, markers of late prophase I and postmeiotic stages were undetectable (Fig. 4E and figs. S4B and S5), further supporting the occurrence of an early meiotic arrest.

To assess the functional consequences of RAD21L deletion, we identified differentially expressed genes (DEGs) in spermatogonia and L/Z primary spermatocytes between WT and KO mice. We detected a mild effect on gene transcription, with a total of 377 DEGs (189 up-regulated and 188 down-regulated) in spermatogonia and 606 DEGs (288 up-regulated and 318 down-regulated) in L/Z primary spermatocytes (Fig. 4, F and G, and tables S5 and S6). Despite the relatively low number of DEGs, these corresponded to key genes involved in spermatogenesis, with a proportion related to infertility phenotypes. In the case of spermatogonia, the DEGs included genes involved in translation [*Rplp1* (35), *Rpl10* (36), and *Rps4x* (36)] and spermatogenesis [*Adcy10* (37) and *Ybx3* (38)]. In primary spermatocytes, DEGs were identified to be involved in spermatogenesis [*Ddx4* (39) and *Tdrd1* (40)], DNA damage response [*Morc2b* (41) and *Mael* (42)], chromatin organization [*Kdm3a* (43) and *Smarca4* (44)], and

cytoskeleton particularly in bouquet and cilium formation [*Tuba3b* (45), *Cfap43* (46), and *Spag6l* (47)] (Fig. 4H and table S7).

Given that the transcriptional profile of spermatogonia was already altered in *Rad21l*-deficient mice, we next examined gene expression changes across spermatogonial subtypes. Differential expression analysis revealed 595 DEGs (380 up-regulated and 215 down-regulated) in differentiating spermatogonia 1 and 384 DEGs (188 up-regulated and 196 down-regulated) in differentiating spermatogonia 2 (fig. S6 and tables S8 and S9). Notably, differentiating spermatogonia 1 exhibited a greater degree of the transcriptomic alterations, with DEGs enriched in pathways related to transcription by RNA polymerase II (e.g., *Mesp1* and *Nfat5*), RNA processing (e.g., *Hspa8* and *Prpf38B*), translation (e.g., *Rpl5* and *Rpl10*), protein homeostasis (e.g., *Bag6* and *Npm1*), spermatogenesis (e.g., *Stra8* and *Ybx3*), and chromatin organization and remodeling (e.g., *Nipbl* and *Stk33*) (fig. S6 and table S10).

This widespread transcriptional misregulation was accompanied by global alterations in chromatin architecture. We observed distinct transcriptional and structural differences between RAD21L-binding genes (9646) and RAD21L-free genes (22,549) (see Materials and Methods and fig. S7). Although overall expression differences between WT and KO primary spermatocytes were modest, RAD21L-binding genes were slightly but significantly up-regulated in KO cells (Mann-Whitney test,  $P < 0.01$ ), whereas RAD21L-free genes were slightly down-regulated (Mann-Whitney test,  $P < 0.01$ ) (fig. S7A). Aggregated Hi-C contact maps further revealed increased and less dispersed interaction frequencies among transcription start site (TSS) of RAD21L-binding genes in KO cells, even for DEGs lacking RAD21L peaks at their promoters (fig. S7B). Further analysis of DEGs in spermatocytes revealed a positive correlation with accessible A compartments and regions undergoing B-to-A compartment switching during prophase I (Fig. 5, A and B). DEGs were also enriched with H3K4me3 histone marks and cohesin-binding TSS but depleted of H3K27ac/H3K27me3, implicating RAD21L in compartmentalization and enhancer-promoter decoupling.

Consistent with our characterization of LRIs, DEGs were positively associated with KO-specific LRIs and negatively associated with both WT-specific and stable LRIs—the latter defined as long-range interactions present in both WT and KO spermatocytes. Notably, KO-specific LRIs were significantly enriched at merged TAD regions, referred to adjacent TADs that appear fused in KO (Fig. 3A), and were also preferentially associated with cohesin-binding sites located at TSSs (Fig. 5, C to E). These findings suggest that the altered chromatin architecture in RAD21L KO cells may facilitate ectopic regulatory interactions, thereby contributing to gene misregulation.

Together, our findings indicate that genome reorganization resulting from RAD21L deletion strongly correlates with transcriptional changes. Dysregulated genes in KO mice were predominantly located within accessible chromatin regions (A compartments enriched in H3K4me3), where the formation of long DNA loops appears to promote novel heterologous long-range interactions, potentially disrupting gene transcription (Fig. 5E).

### Meiotic sex chromosome inactivation is impaired in RAD21L-deficient mice

A defining feature of sex chromosomes is their transcriptional silencing during prophase I, a phenomenon known as meiotic sex chromosome inactivation (MSCI) (48). MSCI is characterized by the accumulation of repressive chromatin modifications in response to asynapsed



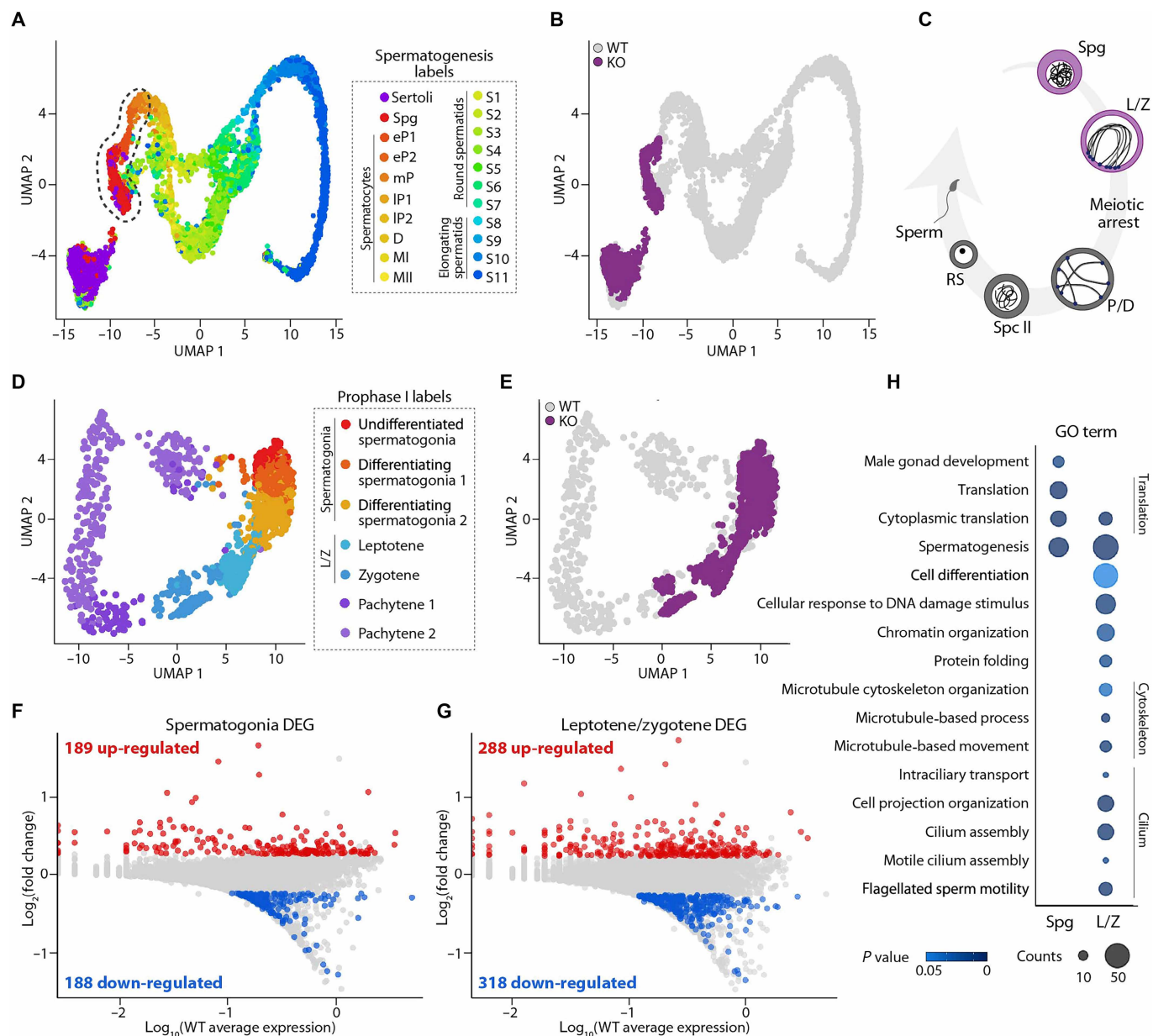


**Fig. 4. Single-cell transcriptome analysis.** (A) Uniform Manifold Approximation and Projection (UMAP) of single-cell RNA-seq data from WT mice, annotated with spermatogenesis stages: spermatogonia, spermatocytes [early prophase 1/2 (eP1/2), mid-prophase (mP), late prophase 1/2 (IP1/2), diplotene (D), metaphase I (MI), and metaphase II (MII)], round spermatids (RSs) (S1 to S7), elongating spermatids (S8 to S11), and Sertoli cells. The dashed circle highlights germ cell stages detected in KO mice. (B) UMAP plot of single-cell RNA-seq data from WT mice (gray) and KO mice (purple). (C) Schematic representation of spermatogenesis progress in KO mice. P/D, pachytene/diplotene; Spc II, secondary spermatocyte. (D) UMAP representation of spermatogonia and early prophase I cells from WT mice, corresponding to cells within the dashed circle in (A). Labels include undifferentiating spermatogonia, differentiating spermatogonia, leptotene, zygotene, and pachytene cells (34). (E) UMAP representation of spermatogonia and early prophase I cells from WT mice (gray) and KO mice (purple), corresponding to cells within the dashed circle in (A). (F) MA plot showing the  $\log_2$  of expression fold change between WT and KO spermatogonia versus average expression in WT spermatogonia. Up-regulated DEGs ( $n = 189$ ) are shown in red, down-regulated DEGs ( $n = 188$ ) in blue, and non-differentially expressed genes (DEGs) in gray. (G) MA plot showing the  $\log_2$  of expression fold change between WT and KO L/Z cells versus average expression in WT L/Z cells. Up-regulated DEGs ( $n = 288$ ) are depicted in red, down-regulated DEGs ( $n = 318$ ) in blue, and non-DEGs in gray. (H) GO analysis of DEGs in spermatogonia and L/Z cells. Bubble size represents the number of genes per GO term.

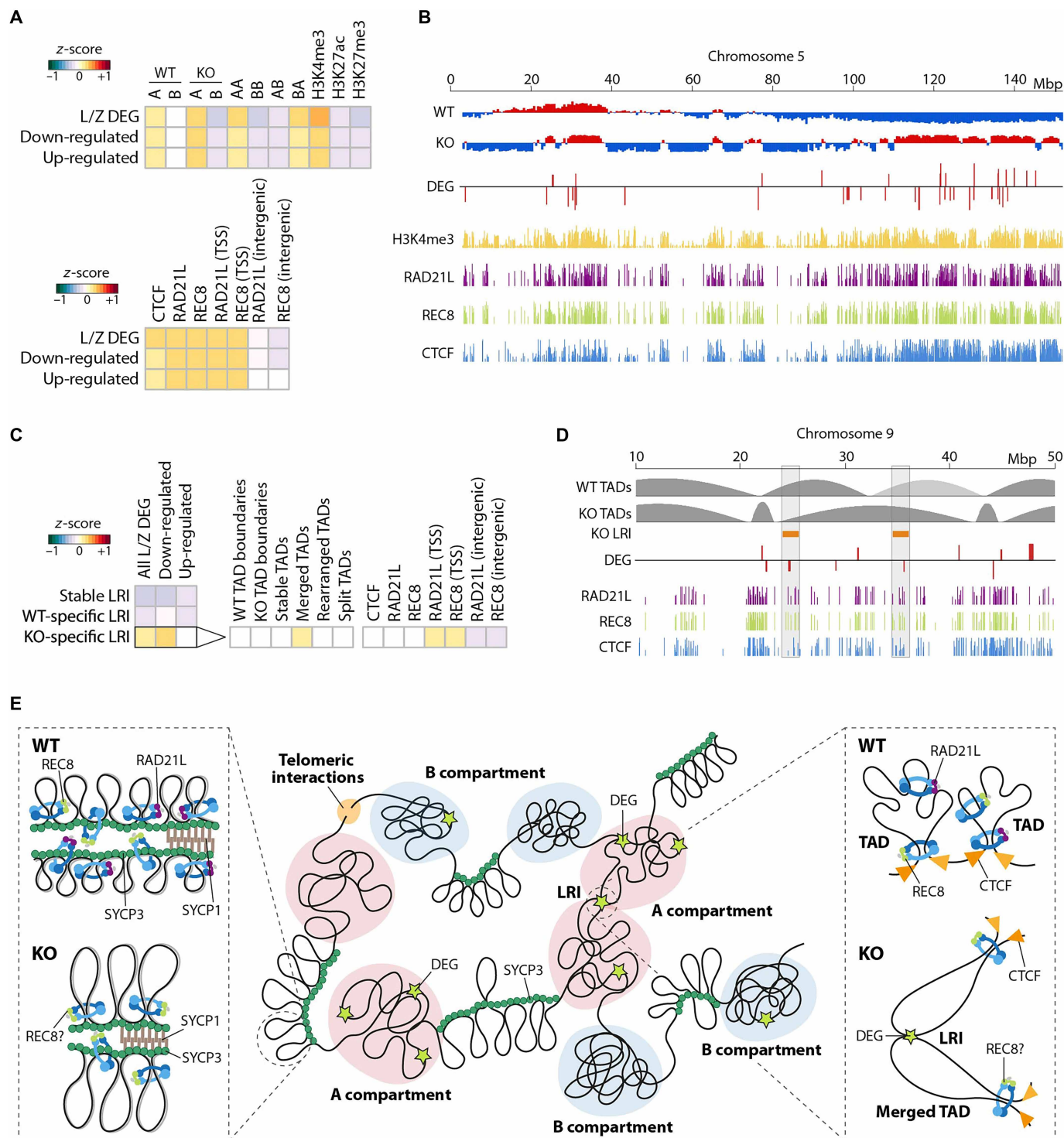


**Fig. 5. Multicomparison genomic analysis.** (A) Multicomparison heatmaps showing pairwise correlations between DEGs in L/Z spermatocytes and various genomic features including compartments in WT and KO mice, compartment switch (see Materials and Methods), histone marks (H3K4me3, H3K27ac, and H3K27me3), CTCF, and cohesin peaks (RAD21L and REC8). (B) Chromosome 5-specific tracks displaying compartments in WT and KO spermatocytes at the L/Z stage,  $\log_2$  fold change of DEGs in L/Z cells, and the distribution of H3K4me3, cohesins (RAD21L and REC8), and CTCF peaks. The observed pattern is consistent across all chromosomes. (C) Multicomparison heatmaps depicting pairwise correlations between LRIs and DEGs, TAD boundaries, TAD categories (as indicated in Fig. 3A), and binding peaks for CTCF and cohesins (RAD21L and REC8). (D) Zoomed-in view of chromosome 9-specific tracks showing TAD distribution in WT and KO spermatocytes at the L/Z stage, KO-specific long-range interactions,  $\log_2$  fold change of DEG expression, and the distribution of cohesins (RAD21L and REC8) and CTCF peaks. (E) Integrative model summarizing the effects of RAD21L deficiency in L/Z cells.



chromatin during prophase I, including the phosphorylation of histone H2AX on serine-139 ( $\gamma$ H2AX). It is known that the X chromosome loses its A-B compartment pattern upon meiosis entry, consistent with MSCI-associated chromatin remodeling, which is translated into an overall reduction in gene expression in primary spermatocytes (1, 10). We found that RAD21L deletion resulted in both structural and functional alterations of the sex chromosomes during meiosis, including abnormal A/B compartmentalization and misregulation of gene expression (Fig. 6). Notably, in KO L/Z spermatocytes, the X chromosome retained a pronounced A/B compartment structure, in stark contrast to WT mice (Fig. 6, A to C). These compartments closely resembled those observed in spermatogonia ( $r^2 = 0.87$ ; Fig. 6C and fig. S8, A to C), indicating a failure to undergo the compartmental attenuation typically associated with MSCI under normal conditions (1). This persistence of somatic-like compartmentalization was also linked to the presence of unusually long DNA loops at short genomic distances in KO mice (Fig. 6B), suggesting broader defects in higher-order chromatin organization and meiotic chromatin remodeling in the X chromosome.

This aberrant higher-order chromatin restructuring was accompanied by up-regulation of genes located on the X and Y chromosomes (Fig. 6D). Specifically, 5.70% of X-linked genes were up-regulated, indicating impaired X chromosome silencing (Fig. 6D, fig. S8D, and table S11). Among the misregulated sex-linked genes were key regulators of spermatogenesis [*Zfy2* (49) and *Taf7l* (50)], as well as genes involved in the DNA damage response [*Fmr1* (51)] (Fig. 6E and table S12). Cytological analysis further revealed impaired accumulation of  $\gamma$ H2AX on sex chromosomes during early prophase I,

consistent with a failure to initiate proper transcriptional silencing (Fig. 6F). Collectively, these findings demonstrate that RAD21L is essential for the regulation of sex chromosome transcriptional repression during meiosis, and its absence leads to widespread misregulation of sex-linked gene expression.

## DISCUSSION

The formation of mammalian germ cells involves extensive chromatin remodeling, orchestrated by regulatory pathways that remain poorly understood. Using an integrative approach combining FACS, Hi-C, and single-cell RNA-seq, we define how RAD21L deficiency disrupts 3D genome architecture and transcriptional regulation in the male germ line. Our results revealed that RAD21L plays multifaceted roles during meiosis, influencing several hierarchical levels of chromatin organization: (i) nuclear compartmentalization, (ii) inter- and intrachromosomal interactions, (iii) long-range interactions, (iv) DNA loop formation, (v) bouquet formation, and (vi) transcriptional regulation of key meiotic genes (Figs. 5E and 7).

RAD21L is a meiosis-specific kleisin subunit of the cohesin complex with all known functions executed as part of this complex rather than independently. It forms a distinct cohesin assembly by associating with SMC3, STAG3, and either SMC1 $\alpha$  or SMC1 $\beta$ , consistent with the established structural paradigm for kleisin-containing cohesins. In this study, we demonstrate that RAD21L is a critical determinant of chromatin structure during early spermatogenesis at multiple levels, not only involved in the formation of TADs and DNA loops but also at the level of A/B compartments, inter/intrachromosomal interactions,

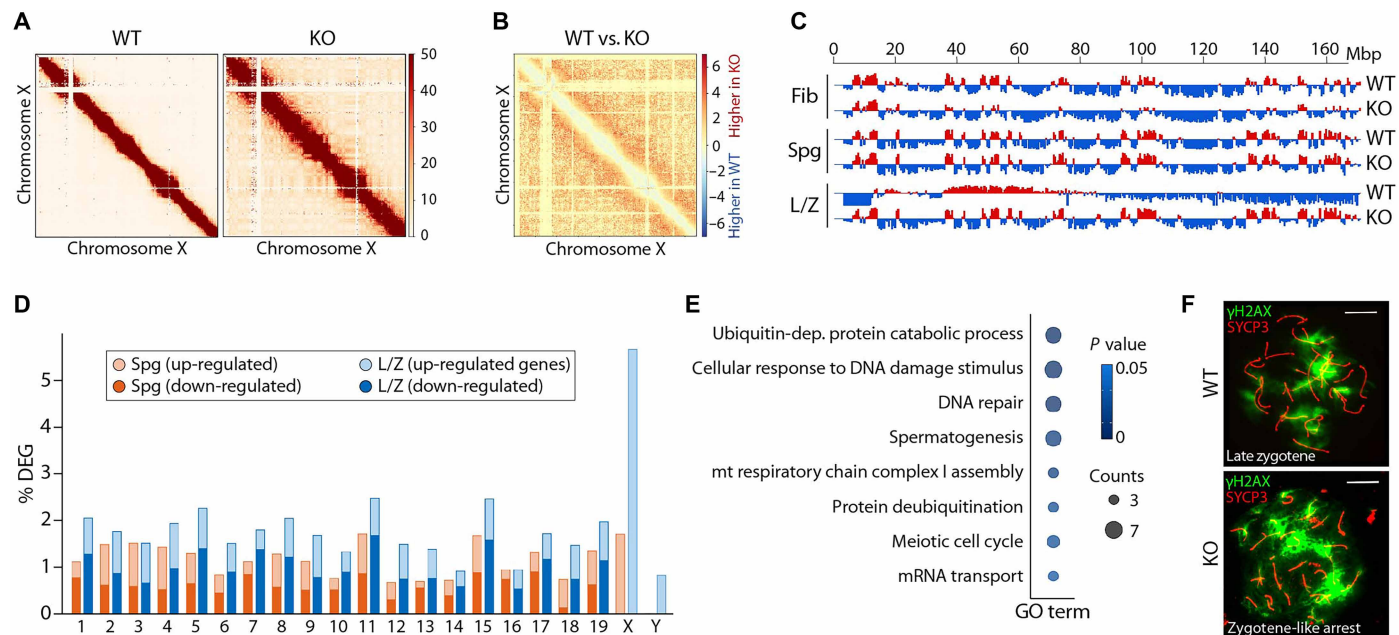


**Fig. 6. Transcriptome misregulation of sex chromosomes.** (A) Chromosome X-specific heatmaps depicting intrachromosomal interactions for L/Z stage cells in WT and KO mice. (B) Differential Hi-C matrix ( $\log_2$  fold change between WT and KO) in L/Z stage cells at 500-kbp resolution. Red indicates increased interactions in KO relative to WT, while blue indicates higher interactions in WT. (C) Compartment signal profiles represented by the first eigenvector along chromosome X across all analyzed cell types and genotypes. (D) Percentage of DEGs relative to the total number of genes in each chromosome, for both spermatogonia and L/Z cells. Dark colors denote down-regulated genes, while lighter colors indicate up-regulated genes. (E) GO analysis of DEGs located on the sex chromosomes in L/Z cells. Bubble size reflects the number of genes per GO term. Only GO terms with more than two genes and a  $P < 0.05$  are shown. mt, mitochondrial. (F) Immunofluorescence images of primary spermatocytes from WT (late zygotene) and KO (zygotene-like) mice labeled with antibodies against  $\gamma$ H2AX (green) and SYCP3 (red). Scale bars, 10  $\mu$ m.

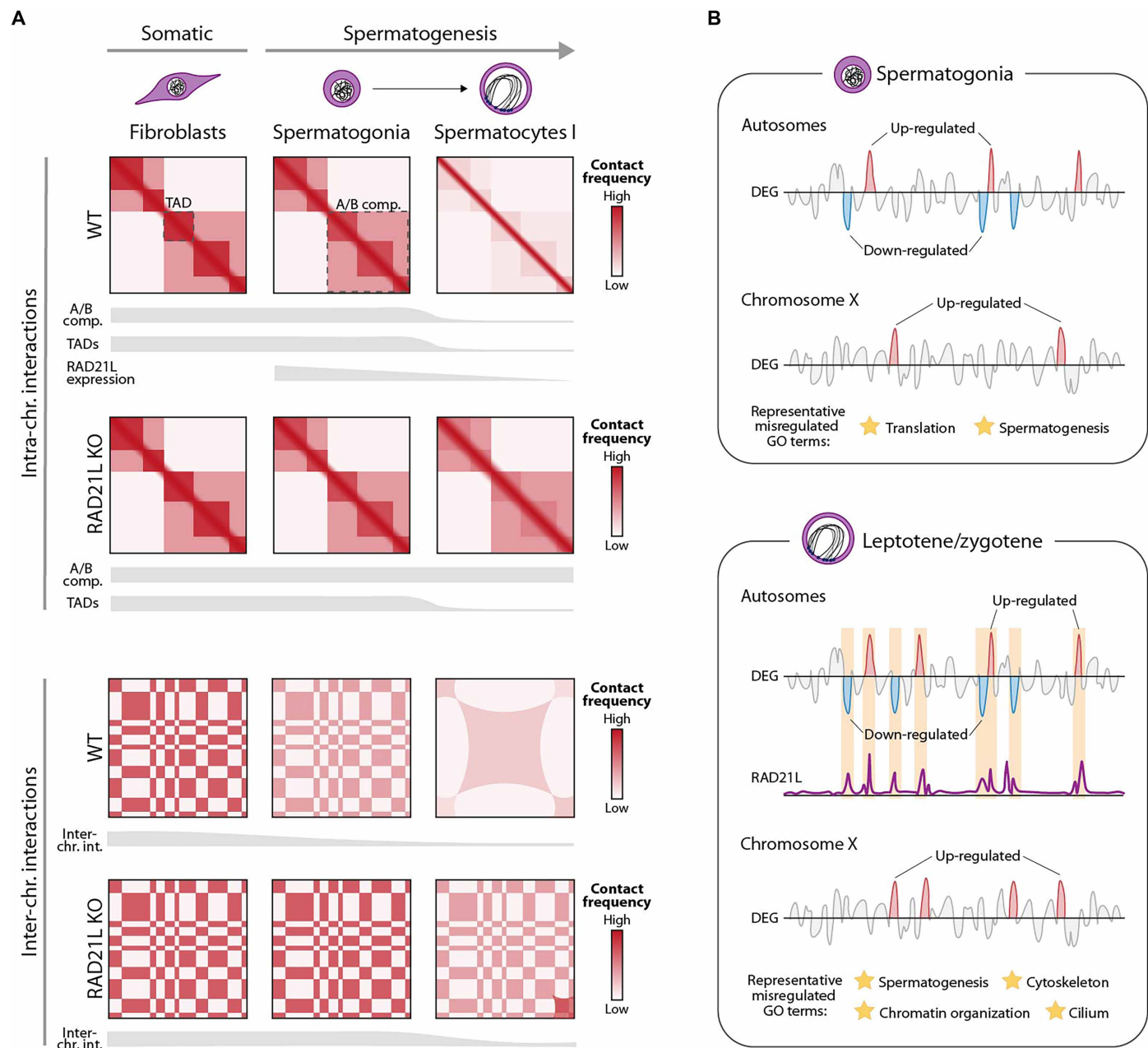


**Fig. 7. Structural and transcriptomic changes in RAD21L-deficient germ cells.** (A) Disruption of chromatin architecture during spermatogenesis in RAD21L-deficient mice. In WT mice, chromatin compartments and TADs are attenuated during prophase I, accompanied by a reduction in interchromosomal interactions. This transition is characterized by a shift from the plaid pattern typical of somatic cells and spermatogonia to an X-shaped configuration in primary spermatocytes. In contrast, KO primary spermatocytes exhibit attenuated TADs but retain compartmentalization and the plaid pattern. In addition, the reduction in interchromosomal interactions is delayed or impaired in both KO spermatogonia and primary spermatocytes. (B) Transcriptomic dysregulation in RAD21L-deficient mice. Loss of RAD21L leads to DEGs in both spermatogonia and primary spermatocytes, with a substantial subset of DEGs in the latter overlapping with RAD21L-binding sites. Although the number of DEGs is relatively modest, they include genes involved in translation, spermatogenesis, chromatin organization, cytoskeleton, and cilium regulation. On the sex chromosomes of KO mice, all DEGs are up-regulated, consistent with partial impairment of MSCI.

and nuclear chromosome occupancy (Fig. 7A). Notably, genomic structural defects were already evident in spermatogonia, underscoring a role for the  $\alpha$ -kleisin in the germ line that is not restricted to meiosis. This observation aligns with earlier reports of *Rad21l* expression, along with other cohesins, in premeiotic spermatogonia (25, 27). Our results provide direct evidence that RAD21L is already

functional in premeiotic cells, albeit at low levels. Its absence results in chromosome decompaction and aberrant interchromosomal interactions, underscoring its critical role in early germ cell development. Collectively, these observations support the notion that RAD21L functions as a germline-specific cohesin, rather than being restricted to meiosis.

As *Rad21l* expression increases during prophase I, we detected further architectural disruptions in early primary spermatocytes. While both WT and KO cells exhibited reduced TAD boundary strength, boundaries marked by RAD21L in WT spermatocytes were notably rearranged in mutants. These findings echo previous observations in mouse one-cell embryos, where deletion of the somatic subunit RAD21 impaired loops and TAD formation (28) and are consistent with studies showing altered chromatin organization following auxin-induced RAD21 degradation in somatic cells (52).

Meiotic cohesins provide a structural foundation for chromosome axis formation (13, 53, 54), as evidenced by discontinuous and fragmented axes observed upon deletion of RAD21L (11, 54). Our study builds on this by revealing that these defects in synaptonemal complex (SC) assembly resulted in the elongation of DNA loops and, notably, enabled the detection of A and B compartments in primary spermatocytes (Fig. 7A)—structures typically attenuated under normal conditions in both adult (1, 3, 10) and juvenile (23) mice. Although shortened chromosomal axes have been previously reported during the first wave of spermatogenesis (55, 56), the extensive defects detected in RAD21L KO juvenile mice are unlikely to be solely attributable to age but to the structural role of RAD21L. Our results mirror previous observations in somatic cells, where cohesin loss results in an increase in genome compartmentalization (57, 58). Similarly, defects in SC assembly and synapsis due to the absence of SYCP2 or TOP6BL also prevent the normal compartment attenuation during meiotic prophase I (2). The presence of A/B compartments in early stages of RAD21L-deficient meiosis was accompanied by alterations in chromosome organization at two hierarchical levels: (i) reduced DNA loops size at short distances (from 0.2 to 10 Mbp) and (ii) increased DNA loop size at long distances (more than 10 Mbp). These structural changes are accompanied by the detection of heterologous long-range interactions in RAD21L mutant spermatocytes. Together with previous cytological evidence of shortened and fragmented LEs with aberrant synapsis (11), our results underscore the role of meiotic cohesin complexes as key determinants of chromatin structure at, at least, two levels. One level entails cohesin-dependent loop and TAD formation, and the other includes nuclear compartmentalization (59). As previously suggested for early embryos, defects in DNA loops upon cohesin deletion can affect long-range interactions by modulating the surface area of chromosomes, leading to changes in interchromosomal interaction frequencies (28).

Furthermore, cohesin deletion also resulted in the impairment of the formation of two other major structural features specific to meiosis: (i) bouquet formation and (ii) MSCI. The formation of the bouquet structure in early prophase I stages is essential for successful synapsis between homologs and proper resolution of recombination events (19, 60, 61), with RAD21L playing a role. We previously showed that *Rad21l*-deficient spermatocytes exhibit disrupted attachment of some telomeres to the nuclear envelope, as evidenced by the presence of internal RAP1 telomeric signals within the nucleus (up to six chromosomes) rather than exclusively at the periphery, as observed in WT (11). It has been proposed that RAD21L cohesins play a role in suppressing intersister SC formation, contributing to homologous chromosome association independently of DSBs (53). Our findings, which reveal an increased presence of aberrant telomeric interactions and KO-specific long-range interactions, provide further evidence in support of this hypothesis.

Likewise, we observed impaired  $\gamma$ H2AX accumulation on sex chromosomes in RAD21L-deficient mice, accompanied by misregulation

of XY-linked genes during early prophase I. It is well established that X chromosome silencing during prophase I is accompanied with distinct higher-order chromatin reorganization, including increased intrachromosomal over interchromosomal interactions, attenuation of compartmentalization, and a reduction in both the number of TADs and associated signal intensity at the onset of prophase I (1, 4). The initiation of MSCI is tightly coupled to meiotic progression, as failure to properly silence the sex chromosomes can trigger apoptosis through activation of meiotic checkpoints (62). Recent studies (63, 64) have provided compelling evidence that transcriptional silencing of the sex chromosomes begins earlier than previously thought, with detectable repression already occurring during leptotema and zygotema. In agreement with this, Ascensão and collaborators (65) demonstrated chromatin remodeling events on sex chromosomes that precede full synapsis, supporting the notion that MSCI is a progressive process initiated before pachynema. Our findings in *Rad21l*-deficient mice are consistent with this emerging view. We propose that the observed meiotic arrest may result from checkpoint activation in response to defective sex chromosome silencing, likely driven by altered chromatin architecture. Supporting this, we detected abnormal X chromosome compartmentalization, characterized by increased mid-range genomic interactions—hallmarks of compromised silencing. In line with these structural changes, transcriptomic analysis revealed elevated expression of both X- and Y-linked genes (Fig. 7B), further indicating disruption of MSCI.

Our findings also highlight a critical role for cohesin in transcriptional regulation within the germ line. While recent studies have demonstrated cohesin's involvement in transcriptional control in somatic cells (66), the mechanisms governing gene expression in the germline remain poorly understood. Acute cohesin deletion in somatic cell lines has been shown to have a minimal impact on gene expression (21, 58, 67–69). Our results partially mirror these observations, revealing widespread but subtle transcriptional misregulation in *Rad21l*-deficient germ cells (Fig. 7B). This dysregulation affects both cohesin-binding and cohesin-free genes (70), resulting in both up- and down-regulation, consistent with previous findings in somatic systems (58). These findings raise important questions regarding the mechanisms by which cohesin-mediated chromatin topology influences transcriptional regulation. Although cohesins have been shown to directly regulate transcription by facilitating enhancer-promoter communication, increasing RNA polymerase II occupancy at genes, or promoting the transition of paused RNA polymerase II into productive elongation (66, 69, 71, 72), the precise molecular remain elusive. In the context of mammalian male germ cells, it was initially proposed that cohesin loading correlates with gene expression and chromatin remodeling (1), with meiotic cohesins preferentially locating to promoter regions (within 2 kbp of TSS) of genes with significantly higher expression compared to genes that lack cohesin peaks at their promoters (1).

Summarizing, we demonstrate that RAD21L deficiency induces transcriptional alterations beginning in premeiotic STRA8-positive cells (i.e., differentiating spermatogonia 1), consistent with the early expression of *Rad21l* and other meiotic genes in an STRA8/MEIOSIN-dependent manner (24–27). Although the genome-wide transcriptional impact was relatively modest in both spermatogonia and primary spermatocytes, the subset of dysregulated genes includes key regulators of spermatogenesis, encompassing pathways related to translation, DNA damage response, and chromatin organization, among others. The observed 3D genome remodeling observed upon



cohesin deletion was accompanied by transcriptional dysregulation of key meiotic genes in both meiotic and premeiotic cells, including *Sycp3*, *Ybx3*, and *Zfy2*. The latter (*Zfy2*) is a known meiotic executioner gene, whose ectopic expression during meiosis results in pachytene arrest and cell death by apoptosis (73). These findings suggest that transcriptional misregulation in differentiating spermatogonia, particularly of genes involved in chromatin organization and remodeling, may exacerbate defects in chromatin architecture even before meiotic entry. Moreover, given that inhibition of the RNA polymerase II activity leads to global chromatin compaction and enhanced segregation of A/B compartments (74), dysregulation of transcription-related genes in differentiating spermatogonia may further hinder proper chromatin remodeling during spermatogenesis. As a result, the combined effect of disrupted chromatin architecture, transcriptional misregulation, partial failure of sex chromosome inactivation, and up-regulation of the meiotic executioner *Zfy2* likely converge to cause meiotic arrest in *Rad21l*-deficient mice.

All in all, our study reveals the dual structural and regulatory roles of meiotic cohesins in orchestrating the extensive chromatin reorganization that occurs during the formation and differentiation of the mammalian male germline. We uncover a previously unidentified mechanistic dimension of RAD21L-containing cohesins, suggesting roles that extend beyond their canonical functions in meiosis. Specifically, RAD21L appears to contribute to germ cell development through regulatory mechanisms distinct from its classical role in assembling the cohesin axis, which supports axial element formation and facilitates synaptonemal complex assembly during chromosome synapsis. While our model does not yet capture the full complexity of protein-protein interactions and additional factors influencing chromatin architecture, our data show that RAD21L deletion alters the behavior of specific genomic regions in a transcription-dependent manner. Further investigations into the mechanisms underlying these changes will provide new insights into how cohesins-mediated 3D genome organization governs gene expression during germ cell formation.

## MATERIALS AND METHODS

### Animals and cell lines

We processed *Rad21l*<sup>−/−</sup> male mice at 15 days postpartum, in which the mutation at the *Rad21l* locus is a null allele produced by gene targeting in a mixed BL6/129 background (11). All animal procedures were approved by the Bioethics Committee of the University of Salamanca and subsequently authorized by the competent authority of the Junta de Castilla y León, Spain (project approval code: 563) in accordance with the European Directive 2010/63/EU on the protection of animals used for scientific purposes and applicable Spanish national legislation (RD 53/2013). This study complies with the ARRIVE 2.0 guidelines and the institutional guidelines from the Consejo Superior de Investigaciones Científicas and the Universidad de Salamanca.

A primary fibroblast cell line was established from a *Rad21l*<sup>−/−</sup> male mouse following standard procedures. Briefly, samples of connective tissue were washed in 1× phosphate-buffered saline (PBS) supplemented with antibiotic-antimycotic solution [penicillin (100 U/ml), streptomycin (100 µg/ml), gentamicin (50 µg/ml), and amphotericin B (0.25 µg/ml)]. Cultures were established by disaggregating tissue with a scalpel blade and resuspending cells in Dulbecco's modified Eagle's medium supplemented with 10% fetal bovine serum. Cell

cultures were incubated at 37°C in 5% CO<sub>2</sub>. Fibroblasts used as a somatic control in Hi-C experiments were cultured until cells reached 100% confluence and then were cross-linked with 1% formaldehyde for 10 min at a concentration of 1 million cells/500 µl. The cross-linking reaction was quenched by adding glycine (0.125 M) and incubating at room temperature (RT) for 5 and 15 min at 4°C. Cells were then incubated with trypsin for 8 min, washed twice with 1× PBS and scrapped. Cells were centrifuged at 1800g for 5 min, and the cell pellet was flash-frozen at −80°C until use.

### Spermatocyte spreads and immunofluorescence

To obtain spermatocyte spreads, testicular biopsies were obtained immediately after dissection and processed, as previously described (75). Basically, a piece of testicular tissue was gently minced on a slide in 1× PBS. Cells were then swollen with 1% Lipsol during 20 min at RT and subsequently fixed with a solution containing 4% paraformaldehyde. After 2 hours, slides were washed in 1% Photo-Flo solution and further processed for immunofluorescence or frozen at −20°C until use.

Immunostaining of spermatocytes was performed as previously described (75) using a mouse antibody against SYCP3 (Santa Cruz Biotechnology, #sc-74569; 1:1000) and a rabbit antibody against γH2AX (Millipore, #07-164; 1:500). Primary antibodies were incubated overnight at 4°C and secondary antibodies for 1 hour at 37°C in a humid chamber. All antibodies were diluted in PBST (0.05% Tween in PBS). After washing away excess, slides were incubated with secondary antibodies: goat Alexa Fluor 555 α-mouse (Thermo Fisher Scientific, #A-32727; 1:200) and goat Alexa Fluor 488 α-rabbit (Jackson ImmunoResearch, #111-547-003; 1:100), and DNA was counterstained with antifade solution (VECTASHIELD) containing DAPI (4',6'-diamidino-2-phenylindole; 8 µg/ml).

### FACS of mouse male germ cells

Testicular disaggregation from RAD21L-deficient mice was conducted as previously described (1). Briefly, decapsulated testis were enzymatically disaggregated with collagenase type II (0.5 mg/ml), trypsin from bovine pancreas (0.75 mg/ml), and DNase I (1 ng/µl) at 33°C for 15 min with agitation. Fetal bovine serum at a final concentration of 5% was then added to the mix to inactivate the trypsin. The cell suspension was filtered through a 70-µm-diameter cell strainer and subsequently centrifuged at 1800g for 3 min. Germ cells were then cross-linked with 1% formaldehyde for 10 min at a concentration of 1 million cells/500 µl. The cross-linking reaction was quenched by adding glycine (0.125 M) and incubating at RT for 5 and 15 min at 4°C. Germ cells were then centrifuged at 1800g for 5 min and dyed in Hoechst 33342 (5 µg/ml) for 30 min at 33°C before FACS or flash-frozen at −80°C until use.

Germ cells were sorted using a BD Influx (BD Biosciences) coupled with an ultraviolet laser (355 nm). Because meiosis arrests at a zygotene-like stage in RAD21L-deficient mice (11, 54), two germ cell populations (spermatogonia and primary spermatocytes at L/Z stages) were isolated according to both their DNA content and their complexity by plotting Hoechst blue (UV355-460/50) versus Hoechst red (UV355-670/30) (fig. S1). Sorted cells were collected in 1× PBS and centrifuged at 1800g for 5 min, and cell pellets were flash-frozen at −80°C until use.

The enrichment of each flow-sorted population was evaluated by the immunodetection of specific meiotic proteins. Spermatogonia were assessed with an anti-CD90.2 antibody (Miltenyi Biotec, #130-102-452;

1:10 dilution) and DAPI morphology, whereas L/Z population was distinguished using a mouse antibody against SYCP3 (Abcam, #97672; 1:200 dilution) and a rabbit antibody against  $\gamma$ H2AX (Sigma-Aldrich, #H5912; 1:400 dilution) (fig. S1). Briefly, an aliquot of cells was fixed on slides with 4% paraformaldehyde for 20 min and further processed for immunofluorescence. Primary antibodies were incubated overnight at 4°C, and secondary antibodies (all from Jackson ImmunoResearch; 1:200 dilution) were incubated for 1 hour at 37°C. DNA was counterstained with antifade solution (VECTASHIELD) containing DAPI (8  $\mu$ g/ml). Slides were analyzed using an epifluorescence microscope (AxioPhot, Zeiss) coupled with a ProgRes CS10plus (Jenoptik camera), and images were captured using ACO XY program (A. Coloma, Open Microscopy). Between 80 and 100 cells from each population were analyzed, and only populations with a cell enrichment above 80% were used in subsequent experiments.

### In nuclei Hi-C

Hi-C libraries were generated following standard procedures (1), generating three biological replicates per each KO germ cell type and one replicate for KO fibroblasts. Briefly, cross-linked populations were incubated in lysis buffer for 30 min in ice and then centrifuged at 2000g for 5 min. Cells were subsequently washed twice with 1× NEBuffer 2 and resuspended in 0.5% SDS in 1× NEBuffer 2. After incubating cells for 10 min at 65°C, 10% Triton X-100 in 1× NEBuffer 2 was added and incubated for 30 min at 37°C. Cells were then centrifuged at 2000g for 5 min and washed twice with 1× NEBuffer 2. Following, chromatin was digested by incubating cells overnight with 400 U of Mbo I at 37°C. An aliquot for the ND (non-digested) control was taken before the restriction enzyme addition, and another aliquot for the NL (nonligated) control was taken from the digested sample the following day. A digestion control was performed by incubating the ND and NL controls with proteinase K (1 mg/ml) for 1 hour at 65°C, followed by phenol:chloroform purification. The digestion quality was checked by running DNA from both controls on a 0.8% agarose gel.

After digestion, cells were centrifuged at 2000g for 5 min and washed twice with 1× NEBuffer 2. Chromatin ends were then repaired and biotinylated by resuspending cells with reparation mix [1× NEBuffer 2, 0.05 mM dCTP, 0.05 mM dTTP, 0.5 mM dGTP, 0.05 mM biotin-dATP, and 50 U of Klenow] and incubating them for 45 min at 37°C. Following, cells were incubated for 10 min at 65°C and centrifuged at 2000g for 5 min. An aliquot for the 3C control was taken before adding the reparation mix. Both the 3C control and the sample were resuspended with ligation buffer [1× NEB T4 ligase buffer, 0.8% Triton X-100, bovine serum albumin (0.1 mg/ml), and 10,000 U of T4 DNA ligase] and incubated overnight at 16°C. The following day, cells were centrifuged at 2000g for 5 min and resuspended in 1× NEBuffer 2 with RNase A (0.25 mg/ml). After incubating cells for 15 min at 37°C, proteinase K (0.5 mg/ml) was added. Cells were then incubated at 65°C overnight to reverse the cross-link. DNA was subsequently purified with phenol:chloroform. DNA quality from the 3C control and the Hi-C sample was assessed by running a 0.8% agarose gel, and DNA concentration was measured by a Qubit.

For library preparation, samples were first sonicated for 30-s on, 90-s off, 4 cycles, and low mode (three times). Subsequently, biotinylated fragments were pulled down using Dynabeads MyOne Streptavidin T1 beads. Briefly, beads were washed with 2× binding buffer [10 mM tris-HCl (pH 7.5), 1 mM EDTA, and 2 M NaCl] and

0.05% Tween 20 in 1× binding buffer. Beads were then resuspended with 1× binding buffer, mixed with the sonicated samples and incubated for 30 min at RT under rotation. After two washes with 1× binding buffer, samples were resuspended with the end repair mix (1× NEB T4 DNA ligase buffer with 10 mM ATP, 0.5 mM dNTP mix, 50 U of NEB T4 PNK, 12 U of T4 DNA polymerase I, and 5 U of Klenow) and incubated for 30 min at RT to repair ends and remove biotin from unligated ends. Beads were then washed twice with 1× binding buffer, resuspended with the dATP attachment mix (1× NEBuffer 2, 0.5 mM dATP, and 2.5 U of NEB Klenow exo minus), and incubated at 37°C for 30 min. Subsequently, beads were washed twice with 1× binding buffer, resuspended in 1× NEB Quick ligation reaction buffer together with the NEBNext adapter and Illumina adapters, and incubated 15 min at RT to ligate adapters to chromatin ends. Following, beads were washed twice with 1× binding buffer, resuspended with tris buffer, and mixed with 1  $\mu$ M primer P5, 1  $\mu$ M primer P7, and cocktail master mix (NEB). A final amplification was performed following the PCR program: 98°C for 30 s; 98°C for 10 s, 60°C for 30 s, and 72°C for 30 s  $\times$  8 cycles; and 72°C for 5 min. The beads were then captured on a magnet, and the supernatants with the amplification products were transferred to a tube. A 1:1 amount of Ampure Beads was added to the samples and incubated for 10 min at RT. The beads were then washed twice with 70% ethanol, eluted with tris buffer, and incubated for 5 min at RT. Ampure Beads were lastly separated on a magnet, and the solution was transferred to a tube. The quality and concentration of the libraries were checked by Qubit and the Agilent Bioanalyzer System. Libraries were submitted for Illumina sequencing (paired-end 150 bp each side on NovaSeq 6000).

### Hi-C data processing, binning, and normalization

BBDuk (version 09/2019) (76) was used for quality check and trimming. Basically, adapters and low-quality reads (i.e., reads with a minimum length of 35 bp and a minimum Phred quality score of 20) were removed. High-quality reads were then mapped against the mouse genome (version mm10) using the GEM (version 3.6.1) mapper (77) from TADbit (version 1.0.1) (32). Reads were iteratively mapped using windows from 15 to 75 bp in 5-bp steps. Possible artifacts were removed using the following filters: “self-circle,” “dangling-end,” “error,” “extra dangling-end,” “too short,” “too large,” “duplicated,” and “random breaks.” The maximum molecule length parameter was set at two times the 99.9 percentile of the insert size distribution, returned by the “insert\_size” from TADbit. The maximum distance of a read to a cleavage site was set to the 99.9 percentile of the insert size distribution.

Binning and data normalization were conducted using an in-house script that imports the “HiC\_data” module of TADbit to bin the reads that passed the filtering step into a square matrix of 50 kbp. Then, 500 kbp matrices were created and subsequently processed with HiCExplorer (version 3.7) (78). All matrices were corrected with ICE (iterative correction and eigenvector decomposition) and normalized to a total of 100 million interaction counts by scaling the sum of all interactions within the matrix. Pairwise correlations were computed between Hi-C replicates (based on the Pearson correlation method) (fig. S1). Normalized matrices were compared using hicCompareMatrices from HiCExplorer, which applies a log<sub>2</sub> ratio between matrices from different genotypes. Normalized matrices and differential matrices (log<sub>2</sub> fold change between WT and KO matrices) were then plotted at a 500-kbp resolution.

### Averaged contact probability $P(s)$ and its slope

Contact probability  $P(s)$  curves were obtained genome-wide from normalized 50-kbp matrices using HiCExplorer. Slopes were calculated as the derivative of the contact probability versus genomic distance curves, and average loop size was estimated as the highest point of the slope as previously described (6, 28).

### Inter- and intrachromosomal interaction analysis

Normalized 500-kbp matrices were transformed into GInteraction tables using HiCExplorer, which includes interaction values between all genomic bins genome-wide. Mean pairwise interchromosomal interactions for each chromosome were plotted as a heatmap where yellow and green colors represent higher interaction levels, whereas dark blue tones represent lower interactions. Mean interactions of interchromosomal and intrachromosomal interactions for each chromosome were also used to calculate inter/intrachromosomal interaction ratios using RStudio. Interchromosomal interactions by pairwise chromosomes were also plotted along chromosome length.

### Intercentromeric and intertelomeric interaction quantification

The GInteraction tables were also used to quantify interchromosomal interactions between centromeres and telomeres. Centromeric regions were defined as the first 3.5 Mb of each chromosome, whereas telomeric regions were defined as the last 3.5 Mb of each chromosome, regardless of chromosomal size. Only interactions between centromeric or telomeric regions of different chromosomes were considered for the quantification of intercentromeric and intertelomeric interactions.

### Long-range interchromosomal interactions

LRIs were defined as previously described (10). Briefly, 500-kbp resolution bins whose SD (z-score) was higher than 2.58, were identified as long-range interchromosomal interactions. The long-range interactions that were detected only in KO mice but not in WT mice were considered KO specific for further analysis. These KO-specific LRIs were plotted using the package RIdeogram (version 0.2.2) (79) from RStudio and CIRCOS (version 0.69-8) (80). Bins of KO-specific LRIs were also intersected against genes from the mouse GENCODE annotation version M23 (mm10) to obtain overlapping genes. These genes were then submitted to a Gene Ontology Enrichment Analysis (GOEA).

### A/B compartmentalization

A/B compartments were defined from the first eigenvector values, which were calculated from normalized 500-kbp matrices using the package FAN-C (version 0.9.14) (33) with default parameters. From the first eigenvector values, 0 was defined as the threshold to differentiate between A and B compartments and average GC content was used to label them. Compartment strength was estimated as the average of the first eigenvector.

A/B compartmentalization was then pairwise compared between genotypes and cell types using 500-kbp bin resolution. Bins were divided into four categories: AA (bins that were A compartments in both genotypes), BB (bins that were B compartments in both genotypes), AB (bins that were A compartments in WT cells but B compartments in KO cells), and BA (bins that were B compartments in WT cells but A compartments in KO cells).

### TAD calling and insulator score

TADs were called from 500-kbp resolution matrices using the function `find_tads` from TADbit with default parameters. TADs were compared between genotypes and classified as stable (when overlapping between TADs was higher than 75%), merged, split, or rearranged. Insulator score was calculated using the package FAN-C (version 0.9.14) (33) following windows of 1 Mbp.

### Single-cell RNA-seq, data processing, filtering, and normalization

Testicular disaggregation from *Rad21*<sup>+/+</sup> and *Rad21*<sup>-/-</sup> mice at 55 days postpartum was conducted as previously described (1). An aliquot of the single-cell solution was loaded into a Chromium Single Cell Chip (10x Genomics), aiming to recover between 5000 and 6000 cells. Libraries were prepared following the manufacturer's instructions and sequenced on Illumina NovaSeq 6000 (50-bp paired ends).

Cell Ranger (version 6.1.2) was used to map the single-cell RNA-seq reads against the mouse annotation (version GRCm39) using default settings. Mapped data were subsequently analyzed with the Seurat package (version 4.3) (81). To avoid the presence of multiplets (i.e., one droplet containing multiple cells), cells with a UMI count exceeding four times of SD from the median were removed. Then, cells expressing less than 500 genes and cells expressing more than 10% of mitochondrial genes were filtered out.

Raw counts were then normalized using the `sctransform` package implemented in Seurat, which calculates Pearson residuals from regularized negative binomial regression. `Sctransform` omits the need of pseudocount addition or log transformation and improves downstream analysis (82).

### Dimensionality reduction, cell type assignment, and data integration

For visualization of single-cell RNA-seq data, dimension reduction was performed on normalized datasets following Uniform Manifold Approximation and Projection (UMAP). For this, the principal components analysis (PCA) was first calculated using the first 50 PCs, and then the UMAP was computed with specific parameters (`dims = 1:50`, `n.neighbors = 100`, and `min.dist = 0.5`).

Cells were labeled using the R package SingleR (version 2.2) (83), which uses a reference dataset with known labels to automatically annotate cells from a given sample by correlating their gene expression. The reference dataset used was ErnstSpermatogenesisData (34), which includes two different approaches to labeling cells: "Cellranger" and "emptyDrops." The Cellranger approach (hereafter spermatogenesis labels) included germ cell types (i.e., spermatogonia, 8 subtypes of primary spermatocytes, and 11 subtypes of spermatids) and somatic cell types (i.e., Sertoli, Leydig, Fetal Leydig, vascular endothelial cells, peritubular myoid cells from the basal lamina, and testicular macrophages). Instead, the emptyDrops approach (hereafter prophase I labels) included more specific labels: three subtypes of spermatogonia and four subtypes of meiotic prophase I. The quality of cell type labeling was checked by plotting a heatmap of the SingleR assignment scores across all cell-label combinations and by plotting expression levels of previously described gene markers (34).

Normalized WT and KO datasets were integrated as previously described (84). Basically, 3000 features were selected for integration,



and then Pearson residuals were calculated. After identifying anchors, datasets were integrated using the `IntegrateData` function, specifying the `sctransform` normalization method. To visualize the integrated object, dimension reduction was performed following UMAP. In this case, the PCA was first calculated using the first 50 PCs, and then the UMAP was computed with specific parameters (`dims = 1:20`, `n.neighbors = 50`, and `min.dist = 0.6`).

### Differential gene expression analysis

Differential gene expression analysis was performed in spermatogonia and L/Z cells comparing WT and KO mice. For the analysis of spermatogonia, cells that were labeled as “undifferentiated spermatogonia,” “differentiating spermatogonia 1,” or “differentiating spermatogonia 2” using the `emptyDrops` approach (34) (prophase I labels) were included. Instead, for the analysis of L/Z cells, only cells labeled as “leptotene” or “zygotene” using the `emptyDrops` approach (34) (prophase I labels) were included.

To detect DEGs between WT and KO cells, the function `FindMarkers` from Seurat was used, specifying the `sctransform` normalization method. Only genes with an absolute  $\log_2$  fold change greater than 0.25 and an adjusted *P* value (with the Benjamini-Hochberg procedure) smaller than 0.05 were considered DEGs. Because KO germ cells were arrested at a zygotene-like stage, spermatid marker genes from S1 to S11 clusters were not included in the analysis. Genomic coordinates from DEGs were then extracted from the mouse GENCODE annotation version M23 (mm10) for subsequent analysis (integration with the Hi-C data and multiassociation analysis).

DEGs were visualized in MA plots representing the  $\log_2$  of expression fold change between WT and KO cells versus average expression in WT cells. These genes were then submitted to a GOEA.

### Classification of RAD21L-binding genes and RAD21L-free genes

Available chromatin immunoprecipitation sequencing (ChIP-seq) data for RAD21L (1) peaks in WT primary spermatocytes were downloaded and processed as previously described (5). Mouse genes were classified using the `subsetByOverlaps` function from the `GenomicRanges` package based on GENCODE annotation version M23 (85). Genes overlapping at least one RAD21L peak were designated as RAD21L-binding genes, while genes lacking RAD21L peaks were classified as RAD21L-free genes.

### Gene ontology enrichment analysis

GOEA was performed using DAVID (86, 87), which identifies enriched Gene Ontology (GO) terms relative to the expected genome background. Only GO terms with at least three genes and an adjusted *P* value (with the Benjamini-Hochberg procedure) lower than 0.05 were considered, unless otherwise specified in the figure legends.

### Multiasociation analysis

Statistical association between different genomic features was performed as previously described (5) using the package `RegioneR` (version 1.26) (88). Pairwise associations were represented as heatmaps where *z*-score values greater than 0 indicate positive association between the two features, whereas *z*-score values lower than 0 indicate a negative association (adjusted *P* < 0.005 in both cases). *Z*-score values equal to 0 indicate no statistical association between the analyzed features (adjusted *P* > 0.005). For the multiassociation

analysis, available data for H3K4me3 (8), H3K27ac (8), H3K27me3 (8), CTCF (1), RAD21L (1), and REC8 (1) in WT primary spermatocytes was downloaded and processed as previously described (5).

### Statistics and reproducibility

In determining sample sizes, we made all possible efforts to minimize animal suffering. To isolate spermatogonia and spermatocytes for Hi-C experiments, the number of mice was determined based on the number of germ cells required for Hi-C (1). When KO mice were used for single-cell RNA-seq, we were mindful of the cost, time, and difficulty obtaining mutant mice of the required genotype. No statistical method was used to predetermine sample size. No data were excluded from the analyses. The experiments were not randomized. The investigators were not blinded to allocation during experiments and outcome assessment.

Statistical analysis and *P* values are displayed in each plot or specified in the figure legends. In all cases, statistical significance was considered for *P* < 0.05, unless otherwise specified. For box plots, line represents median, box represents 25th to 75th percentile, and whiskers represent 1.5× interquartile range. Statistical significances were determined using two-sided Mann-Whitney *U* tests because data were not normally distributed (Shapiro-Wilk test, *P* > 0.05).

### Supplementary Materials

This PDF file includes:

Figs. S1 to S8

Tables S1 to S12

### REFERENCES AND NOTES

1. C. Vara, A. Paytuví-Gallart, Y. Cuartero, F. Le Dily, F. García, J. Salvà-Castro, L. Gómez-H, E. Julià, C. Moutinho, R. Aiese Cigliano, W. Sanseverino, O. Fornas, A. M. Pendás, H. Heyn, P. D. Waters, M. A. Martí-Renom, A. Ruiz-Herrera, Three-dimensional genomic structure and cohesin occupancy correlate with transcriptional activity during spermatogenesis. *Cell Rep.* **28**, 352–367.e9 (2019).
2. Y. Wang, H. Wang, Y. Zhang, Z. Du, W. Si, S. Fan, D. Qin, M. Wang, Y. Duan, L. Li, Y. Jiao, Y. Li, Q. Wang, Q. Shi, X. Wu, W. Xie, Reprogramming of meiotic chromatin architecture during spermatogenesis. *Mol. Cell* **73**, 547–561.e6 (2019).
3. L. Patel, R. Kang, S. C. Rosenberg, Y. Qiu, R. Raviram, S. Chee, R. Hu, B. Ren, F. Cole, K. D. Corbett, Dynamic reorganization of the genome shapes the recombination landscape in meiotic prophase. *Nat. Struct. Mol. Biol.* **26**, 164–174 (2019).
4. K. G. Alavattam, S. Maezawa, A. Sakashita, H. Khoury, A. Barski, N. Kaplan, S. H. Namekawa, Attenuated chromatin compartmentalization in meiosis and its maturation in sperm development. *Nat. Struct. Mol. Biol.* **26**, 175–184 (2019).
5. L. Álvarez-González, F. Burden, D. Doddamani, R. Malinverni, E. Leach, C. Marín-García, L. Marín-Gual, A. Gubern, C. Vara, A. Paytuví-Gallart, M. Buschbeck, P. J. I. Ellis, M. Farré, A. Ruiz-Herrera, 3D chromatin remodelling in the germ line modulates genome evolutionary plasticity. *Nat. Commun.* **13**, 2608 (2022).
6. L. Álvarez-González, C. Arias-Sardá, L. Montes-España, L. Marín-Gual, C. Vara, N. C. Lister, Y. Cuartero, F. García, J. Deakin, M. B. Renfree, T. J. Robinson, M. A. Martí-Renom, P. D. Waters, M. Farré, A. Ruiz-Herrera, Principles of 3D chromosome folding and evolutionary genome reshuffling in mammals. *Cell Rep.* **41**, (2022).
7. C. Vara, A. Ruiz-Herrera, Unpacking chromatin remodelling in germ cells: Implications for development and evolution. *Trends Genet.* **38**, 422–425 (2022).
8. S. S. Hammoud, D. H. P. Low, C. Yi, D. T. Carrell, E. Guccione, B. R. Cairns, Chromatin and transcription transitions of mammalian adult germline stem cells and spermatogenesis. *Cell Stem Cell* **15**, 239–253 (2014).
9. A. N. Shami, X. Zheng, S. K. Munyoki, Q. Ma, G. L. Manske, C. D. Green, M. Sukhwani, K. E. Orwig, J. Z. Li, S. S. Hammoud, Single-cell RNA sequencing of human, macaque, and mouse testes uncovers conserved and divergent features of mammalian spermatogenesis. *Dev. Cell* **54**, 529–547.e12 (2020).
10. C. Vara, A. Paytuví-Gallart, Y. Cuartero, L. Álvarez-González, L. Marín-Gual, F. García, B. Florit-Sabater, L. Capilla, R. A. Sánchez-Guillén, Z. Sarrate, R. Aiese Cigliano, W. Sanseverino, J. B. Searle, J. Ventura, M. A. Martí-Renom, F. Le Dily, A. Ruiz-Herrera, The impact of chromosomal fusions on 3D genome folding and recombination in the germ line. *Nat. Commun.* **12**, 2981 (2021).

11. Y. Herrán, C. Gutiérrez-Caballero, M. Sánchez-Martín, T. Hernández, A. Viera, J. L. Barbero, E. De Álava, D. G. De Rooij, J. A. Suja, E. Llano, A. M. Pendás, The cohesin subunit RAD21L functions in meiotic synapsis and exhibits sexual dimorphism in fertility. *EMBO J.* **30**, 3091–3105 (2011).
12. U. Biswas, K. Hempel, E. Llano, A. Pendas, R. Jessberger, Distinct roles of meiosis-specific cohesin complexes in mammalian spermatogenesis. *PLOS Genet.* **12**, e1006389 (2016).
13. E. Llano, Y. Herrán, I. García-Tuñón, C. Gutiérrez-Caballero, E. de Álava, J. L. Barbero, J. Schimenti, D. G. de Rooij, M. Sánchez-Martín, A. M. Pendás, Meiotic cohesin complexes are essential for the formation of the axial element in mice. *J. Cell Biol.* **197**, 877–885 (2012).
14. F. McNicoll, M. Stevense, R. Jessberger, “Cohesin in gametogenesis,” in *Current Topics in Developmental Biology* (Academic Press Inc., 2013), vol. 102, pp. 1–34.
15. S. A. Schalbetter, G. Fudenberg, J. Baxter, K. S. Pollard, M. J. Neale, Principles of meiotic chromosome assembly revealed in *S. cerevisiae*. *Nat. Commun.* **10**, 4795 (2019).
16. M. Rong, A. Matsuda, Y. Hiraoka, J. Lee, Meiotic cohesin subunits RAD21L and REC8 are positioned at distinct regions between lateral elements and transverse filaments in the synaptonemal complex of mouse spermatocytes. *J. Reprod. Dev.* **62**, 623–630 (2016).
17. J. Lee, T. Hirano, RAD21L, a novel cohesin subunit implicated in linking homologous chromosomes in mammalian meiosis. *J. Cell Biol.* **192**, 263–276 (2011).
18. H. Shibuya, Y. Watanabe, The meiosis specific modification of mammalian telomeres. *Cell Cycle* **13**, 2024–2028 (2014).
19. R. Reig-Viader, M. Vila-Cejudo, V. Vitelli, R. Buscà, M. Sabaté, E. Giulotto, M. G. Caldés, A. Ruiz-Herrera, Telomeric repeat-containing RNA (TERRA) and telomerase are components of telomeres during mammalian gametogenesis. *Biol. Reprod.* **90**, 103 (2014).
20. S. Cuartero, F. D. Weiss, G. Dharmalingam, Y. Guo, E. Ing-Simmons, S. Masella, I. Robles-Rebollo, X. Xiao, Y.-F. Wang, I. Barozzi, D. Djeghloul, M. T. Amano, H. Niskanen, J. Paretto, R. D. Dowell, K. Tachibana, M. U. Kaikonen, K. A. Nasmyth, B. Lenhard, G. Natoli, A. G. Fisher, M. Merkenschlager, Control of inducible gene expression links cohesin to hematopoietic progenitor self-renewal and differentiation. *Nat. Immunol.* **19**, 932–941 (2018).
21. N. Q. Liu, M. Maresca, T. van den Brand, L. Braccioli, M. M. G. A. Schijns, H. Teunissen, B. G. Bruneau, E. Nora, E. de Wit, WAPL maintains a cohesin loading cycle to preserve cell-type-specific distal gene regulation. *Nat. Genet.* **53**, 100–109 (2021).
22. M. J. Thiecke, G. Wutz, M. Muhar, W. Tang, S. Bevan, V. Malysheva, R. Stocsits, T. Neumann, J. Zuber, P. Fraser, S. Schoenfelder, J. M. Peters, M. Spivakov, Cohesin-dependent and -independent mechanisms mediate chromosomal contacts between promoters and enhancers. *Cell Rep.* **37**, 107929 (2020).
23. W. Zuo, G. Chen, Z. Gao, S. Li, Y. Chen, C. Huang, J. Chen, Z. Chen, M. Lei, Q. Bian, Stage-resolved Hi-C analyses reveal meiotic chromosome organizational features influencing homolog alignment. *Nat. Commun.* **12**, 5827 (2021).
24. F. K. M. Cheung, C.-W. A. Feng, C. Crisp, Y. Mishina, C. M. Spiller, J. Bowles, BMP and STRA8 act collaboratively to ensure correct mitotic-to-meiotic transition in the fetal mouse ovary. *Development* **152**, DEV204227 (2025).
25. K. Ishiguro, Mechanisms of meiosis initiation and meiotic prophase progression during spermatogenesis. *Mol. Aspects Med.* **97**, 101282 (2024).
26. N. G. Pfaltzgraff, B. Liu, D. G. de Rooij, D. C. Page, M. M. Mikedis, Destabilization of mRNAs enhances competence to initiate meiosis in mouse spermatogenic cells. *Development* **151**, dev202740 (2024).
27. M. L. Kojima, D. G. de Rooij, D. C. Page, Amplification of a broad transcriptional program by a common factor triggers the meiotic cell cycle in mice. *eLife* **8**, e43738 (2019).
28. J. Gassler, H. B. Brandão, M. Imakaev, I. M. Flyamer, S. Ladstätter, W. A. Bickmore, J. Peters, L. A. Mirny, K. Tachibana, A mechanism of cohesin-dependent loop extrusion organizes zygotic genome architecture. *EMBO J.* **36**, 3600–3618 (2017).
29. H. Scherthan, S. Weich, H. Schwegler, C. Heyting, M. Härle, T. Cremer, Centromere and telomere movements during early meiotic prophase of mouse and man are associated with the onset of chromosome pairing. *J. Cell Biol.* **134**, 1109–1125 (1996).
30. R. Reig-Viader, M. Garcia-Caldés, A. Ruiz-Herrera, Telomere homeostasis in mammalian germ cells: A review. *Chromosoma* **125**, 337–351 (2016).
31. B. Liebe, M. Alsheimer, C. Höög, R. Benavente, H. Scherthan, Telomere attachment, meiotic chromosome condensation, pairing, and bouquet stage duration are modified in spermatocytes lacking axial elements. *Mol. Biol. Cell* **15**, 827–837 (2004).
32. F. Serra, D. Bäu, M. Goodstadt, D. Castillo, G. J. Filion, M. A. Marti-Renom, Automatic analysis and 3D-modelling of Hi-C data using TADbit reveals structural features of the fly chromatin colors. *PLOS Comput. Biol.* **13**, e1005665 (2017).
33. K. Kruse, C. B. Hug, J. M. Vaquerizas, FAN-C: A feature-rich framework for the analysis and visualisation of chromosome conformation capture data. *Genome Biol.* **21**, 303 (2020).
34. C. Ernst, N. Eling, C. P. Martinez-Jimenez, J. C. Marioni, D. T. Odum, Staged developmental mapping and X chromosome transcriptional dynamics during mouse spermatogenesis. *Nat. Commun.* **10**, 1251 (2019).
35. L. Perucho, A. Artero-Castro, S. Guerrero, S. Ramón y Cajal, M. E. Lleonart, Z. Q. Wang, RPLP1, a crucial ribosomal protein for embryonic development of the nervous system. *PLOS ONE* **9**, e99956 (2014).
36. D. Swathi, L. Ramya, S. S. Archana, M. Lavanya, B. Krishnappa, B. K. Binsila, S. Selvaraju, X chromosome-linked genes in the mature sperm influence semen quality and fertility of breeding bulls. *Gene* **839**, 146727 (2022).
37. K. C. Hess, B. H. Jones, B. Marquez, Y. Chen, T. S. Ord, M. Kamenetsky, C. Miyamoto, J. H. Zippin, G. S. Kopf, S. S. Suarez, L. R. Levin, C. J. Williams, J. Buck, S. B. Moss, The “soluble” adenyl cyclase in sperm mediates multiple signaling events required for fertilization. *Dev. Cell* **9**, 249–259 (2005).
38. E. Snyder, R. Soundararajan, M. Sharma, A. Dearth, B. Smith, R. E. Braun, Compound heterozygosity for Y box proteins causes sterility due to loss of translational repression. *PLOS Genet.* **11**, e1005690 (2015).
39. S. S. Tanaka, Y. Toyooka, R. Akasu, Y. Katoh-Fukui, Y. Nakahara, R. Suzuki, M. Yokoyama, T. Noce, The mouse homolog of *Drosophila Vasa* is required for the development of male germ cells. *Genes Dev.* **14**, 841–853 (2000).
40. S. Chuma, M. Hosokawa, K. Kitamura, S. Kasai, M. Fujioka, M. Hiyoshi, K. Takamune, T. Noce, N. Nakatsuji, Tdrd1/Mtr-1, a tudor-related gene, is essential for male germ-cell differentiation and nuage/germinal granule formation in mice. *Proc. Natl. Acad. Sci. U.S.A.* **103**, 15894–15899 (2006).
41. B. Shi, J. Xue, J. Zhou, S. D. Kasowitz, Y. Zhang, G. Liang, Y. Guan, Q. Shi, M. Liu, J. Sha, X. Huang, P. J. Wang, MORC2B is essential for meiotic progression and fertility. *PLOS Genet.* **14**, e1007175 (2018).
42. S. F. C. Soper, G. W. van der Heijden, T. C. Hardiman, M. Goodheart, S. L. Martin, P. de Boer, A. Bortvin, Mouse maelstrom, a component of nuage, is essential for spermatogenesis and transposon repression in meiosis. *Dev. Cell* **15**, 285–297 (2008).
43. I. Kasioulis, H. M. Syred, P. Tate, A. Finch, J. Shaw, A. Seawright, M. Fuszard, C. H. Botting, S. Shirran, I. R. Adams, I. J. Jackson, V. Van Heyningen, P. L. Yeyati, Kdm3a lysine demethylase is an Hsp90 client required for cytoskeletal rearrangements during spermatogenesis. *Mol. Cell Biol.* **25**, 1216–1233 (2014).
44. A. Abedini, D. A. Landry, A. D. MacAulay, H. Vaishnav, A. Parbhakar, D. Ibrahim, R. Salehi, V. Maranda, E. MacDonald, B. C. Vanderhyden, SWI/SNF chromatin remodeling subunit Smarca4/BRG1 is essential for female fertility. *Biol. Reprod.* **108**, 279–291 (2023).
45. M. S. Akter, M. Hada, D. Shikata, G. Watanabe, A. Ogura, S. Matoba, CRISPR/Cas9-based genetic screen of SCNT-reprogramming resistant genes identifies critical genes for male germ cell development in mice. *Sci. Rep.* **11**, 15438 (2021).
46. S. Tang, X. Wang, W. Li, X. Yang, Z. Li, W. Liu, C. Li, Z. Zhu, L. Wang, J. Wang, L. Zhang, X. Sun, E. Zhi, H. Wang, H. Li, L. Jin, Y. Luo, J. Wang, S. Yang, F. Zhang, Biallelic mutations in *CFAP43* and *CFAP44* cause male infertility with multiple morphological abnormalities of the sperm flagella. *Am. J. Hum. Genet.* **100**, 854–864 (2017).
47. R. Sapiro, I. Kostetskii, P. Olds-Clarke, G. L. Gerton, G. L. Radice, J. F. Strauss, Male infertility, impaired sperm motility, and hydrocephalus in mice deficient in sperm-associated antigen 6. *Mol. Cell Biol.* **22**, 6298–6305 (2002).
48. J. M. A. Turner, S. K. Mahadevaiah, O. Fernandez-Capetillo, A. Nussenzweig, X. Xu, C. X. Deng, P. S. Burgoyne, Silencing of unsynapsed meiotic chromosomes in the mouse. *Nat. Genet.* **37**, 41–47 (2005).
49. Y. Yamauchi, T. Matsumura, J. Bakse, H. Holmlund, G. Blanchet, E. Carrot, M. Ikawa, M. A. Ward, Loss of mouse Y chromosome gene Zfy1 and Zfy2 leads to spermatogenesis impairment, sperm defects, and infertility. *Biol. Reprod.* **106**, 1312–1326 (2022).
50. A. Moreno-Irusta, E. M. Dominguez, K. Iqbal, X. Zhang, N. Wang, M. J. Soares, TAF7L regulates early stages of male germ cell development in the rat. *FASEB J.* **38**, e23376 (2024).
51. L. M. Pastore, J. Johnson, The *FMR1* gene, infertility, and reproductive decision-making: A review. *Front. Genet.* **5**, 195 (2014).
52. G. Wutz, C. Várnai, K. Nagasaka, D. A. Cisneros, R. R. Stocsits, W. Tang, S. Schoenfelder, G. Jessberger, M. Muhar, M. J. Hossain, N. Walther, B. Koch, M. Kueblbeck, J. Ellenberg, J. Zuber, P. Fraser, J. Peters, Topologically associating domains and chromatin loops depend on cohesin and are regulated by CTCF, WAPL, and PDS5 proteins. *EMBO J.* **36**, 3573–3599 (2017).
53. K. I. Ishiguro, The cohesin complex in mammalian meiosis. *Genes Cells* **24**, 6–30 (2019).
54. K. I. Ishiguro, J. Kim, H. Shibuya, A. Hernández-Hernández, A. Suzuki, T. Fukagawa, G. Shioi, H. Kiyonari, X. C. Li, J. Schimenti, C. Höög, Y. Watanabe, Meiosis-specific cohesin mediates homolog recognition in mouse spermatocytes. *Genes Dev.* **28**, 594–607 (2014).
55. L. A. Vrooman, S. I. Nagaoka, T. J. Hassold, P. A. Hunt, Evidence for paternal age-related alterations in meiotic chromosome dynamics in the mouse. *Genetics* **196**, 385–396 (2014).
56. M. J. Zelazowski, M. Sandoval, L. Paniker, H. M. Hamilton, J. Han, M. A. Gribbell, R. Kang, F. Cole, Age-dependent alterations in meiotic recombination cause chromosome segregation errors in spermatocytes. *Cell* **171**, 601–614.e13 (2017).
57. W. Schwarzer, N. Abdennur, A. Goloborodko, A. Pekowska, G. Fudenberg, Y. Loe-Mie, N. A. Fonseca, W. Huber, C. H. Haering, L. Mirny, F. Spitz, Two independent modes of chromatin organization revealed by cohesin removal. *Nature* **551**, 51–56 (2017).
58. S. S. P. Rao, S. C. Huang, B. G. S. Hilaire, J. M. Engreitz, E. M. Perez, K. R. Kieffer-Kwon, A. L. Sanborn, S. E. Johnstone, G. D. Bascom, I. D. Bochkov, X. Huang, M. S. Shamim, J. Shin, D. Turner, Z. Ye, A. D. Omer, J. T. Robinson, T. Schlick, B. E. Bernstein, R. Casellas,

- E. S. Lander, E. L. Aiden, Cohesin loss eliminates all loop domains. *Cell* **171**, 305–320.e24 (2017).
59. J. H. Haarhuis, B. D. Rowland, Cohesin: Building loops, but not compartments. *EMBO J.* **36**, 3549–3551 (2017).
60. K. A. Boateng, M. A. Bellani, I. V. Gregoret, F. Pratto, R. D. Camerini-Otero, Homologous pairing preceding SPO11-mediated double-strand breaks in mice. *Dev. Cell* **24**, 196–205 (2013).
61. J. Link, D. Jahn, J. Schmitt, E. Göb, J. Baar, S. Ortega, R. Benavente, M. Alsheimer, The meiotic nuclear lamina regulates chromosome dynamics and promotes efficient homologous recombination in the mouse. *PLOS Genet.* **9**, e1003261 (2013).
62. Y. Ichijima, H. S. Sin, S. H. Namekawa, Sex chromosome inactivation in germ cells: Emerging roles of DNA damage response pathways. *Cell. Mol. Life Sci.* **69**, 2559–2572 (2012).
63. X. Lau, P. Munusamy, M. J. Ng, M. Sangrithi, Single-cell RNA sequencing of the cynomolgus macaque testis reveals conserved transcriptional profiles during mammalian spermatogenesis. *Dev. Cell* **54**, 548–566.e7 (2020).
64. A. K. Alexander, E. J. Rice, J. Lujic, L. E. Simon, S. Tanis, G. Barshad, L. Zhu, J. Lama, P. E. Cohen, C. G. Danko, A-MYB and BRDT-dependent RNA polymerase II pause release orchestrates transcriptional regulation in mammalian meiosis. *Nat. Commun.* **14**, 1753 (2023).
65. C. F. R. Ascensão, J. R. Sims, A. Dziubek, W. Comstock, E. A. Fogarty, J. Badar, R. Freire, A. Grimson, R. S. Weiss, P. E. Cohen, M. Smolka, A TOPBP1 allele causing male infertility uncouples XY silencing dynamics from sex body formation. *eLife* **12**, RP90887 (2024).
66. N. L. Rittenhouse, J. M. Downen, Cohesin regulation and roles in chromosome structure and function. *Curr. Opin. Genet. Dev.* **85**, 102159 (2024).
67. E. P. Nora, A. Goloborodko, A.-L. Valton, J. H. Gibcus, A. Uebbersohn, N. Abdennur, J. Dekker, L. A. Mirny, B. G. Bruneau, Targeted degradation of CTCF decouples local insulation of chromosome domains from genomic compartmentalization. *Cell* **169**, 930–944.e22 (2017).
68. J. H. I. Haarhuis, R. H. van der Weide, V. A. Blomen, J. O. Yáñez-Cuna, M. Amendola, M. S. van Ruiten, P. H. L. Krijger, H. Teunissen, R. H. Medema, B. van Steensel, T. R. Brummelkamp, E. de Wit, B. D. Rowland, The cohesin release factor WAPL restricts chromatin loop extension. *Cell* **169**, 693–707.e14 (2017).
69. T. H. S. Hsieh, C. Cattoglio, E. Slobodyanyuk, A. S. Hansen, X. Darzacq, R. Tjian, Enhancer–promoter interactions and transcription are largely maintained upon acute loss of CTCF, cohesin, WAPL or YY1. *Nat. Genet.* **54**, 1919–1932 (2022).
70. S. Sofueva, E. Yaffe, W. C. Chan, D. Georgopoulou, M. Vietri Rudan, H. Mira-Bontenbal, S. M. Pollard, G. P. Schroth, A. Tanay, S. Hadjir, Cohesin-mediated interactions organize chromosomal domain architecture. *EMBO J.* **32**, 3119–3129 (2013).
71. C. A. Schaaf, H. Kwak, A. Koenig, Z. Misulovin, D. W. Gohara, A. Watson, Y. Zhou, J. T. Lis, D. Dorsett, Genome-wide control of RNA polymerase II activity by cohesin. *PLOS Genet.* **9**, e1003382 (2013).
72. S. Oh, J. Shao, J. Mitra, F. Xiong, M. D'Antonio, R. Wang, I. Garcia-Bassets, Q. Ma, X. Zhu, J. H. Lee, S. J. Nair, F. Yang, K. Ohgi, K. A. Frazer, Z. D. Zhang, W. Li, M. G. Rosenfeld, Enhancer release and retargeting activates disease-susceptibility genes. *Nature* **595**, 735–740 (2021).
73. V. V. Subramanian, A. Hochwagen, The meiotic checkpoint network: Step-by-step through meiotic prophase. *Cold Spring Harb. Perspect. Biol.* **6**, a016675–a016675 (2014).
74. M. V. Nguembor, L. Martin, Á. Castells-García, P. A. Gómez-García, C. Vicario, D. Carnevali, J. AlHaj Abed, A. Granados, R. Sebastian-Perez, F. Sottile, J. Solon, C.-T. Wu, M. Lakadamyali, M. P. Cosma, Transcription-mediated supercoiling regulates genome folding and loop formation. *Mol. Cell* **81**, 3065–3081.e12 (2021).
75. L. Marín-Gual, L. González-Rodelas, G. Pujol, C. Vara, M. Martín-Ruiz, S. Berrios, R. Fernández-Donoso, A. Pask, M. B. Renfree, J. Page, P. D. Waters, A. Ruiz-Herrera, Strategies for meiotic sex chromosome dynamics and telomeric elongation in Marsupials. *PLOS Genet.* **18**, e1010040 (2022).
76. B. Bushnell, *BBMap: A Fast, Accurate, Splice-Aware Aligner* (Department of Energy. Joint Genome Institute, 2014).
77. S. Marco-Sola, M. Sammeth, R. Guigó, P. Ribeca, The GEM mapper: Fast, accurate and versatile alignment by filtration. *Nat. Methods* **9**, 1185–1188 (2012).
78. F. Ramírez, V. Bhardwaj, L. Arrigoni, K. C. Lam, B. A. Grüning, J. Villaveces, B. Habermann, A. Akhtar, T. Manke, High-resolution TADs reveal DNA sequences underlying genome organization in flies. *Nat. Commun.* **9**, 189 (2018).
79. Z. Hao, D. Lv, Y. Ge, J. Shi, D. Weijers, G. Yu, J. Chen, *Rldeogram*: Drawing SVG graphics to visualize and map genome-wide data on the ideograms. *PeerJ Comput. Sci.* **6**, e251 (2020).
80. M. Krzywinski, J. Schein, I. Birol, J. Connors, R. Gascoyne, D. Horsman, S. J. Jones, M. A. Marra, Circos: An information aesthetic for comparative genomics. *Genome Res.* **19**, 1639–1645 (2009).
81. R. Satija, J. A. Farrell, D. Gennert, A. F. Schier, A. Regev, Spatial reconstruction of single-cell gene expression data. *Nat. Biotechnol.* **33**, 495–502 (2015).
82. C. Hafemeister, R. Satija, Normalization and variance stabilization of single-cell RNA-seq data using regularized negative binomial regression. *Genome Biol.* **20**, 296 (2019).
83. D. Aran, A. P. Looney, L. Liu, E. Wu, V. Fong, A. Hsu, S. Chak, R. P. Naikawadi, P. J. Wolters, A. R. Abate, A. J. Butte, M. Bhattacharya, Reference-based analysis of lung single-cell sequencing reveals a transitional profibrotic macrophage. *Nat. Immunol.* **20**, 163–172 (2019).
84. A. Singh, B. P. Hermann, “Bulk and single-cell RNA-seq analyses for studies of spermatogonia” in *Methods in Molecular Biology* (Humana Press Inc., 2023), vol. 2656, pp. 37–70.
85. M. Lawrence, W. Huber, H. Pagès, P. Aboyoun, M. Carlson, R. Gentleman, M. T. Morgan, V. J. Carey, Software for computing and annotating genomic ranges. *PLOS Comput. Biol.* **9**, e1003118 (2013).
86. D. W. Huang, B. T. Sherman, R. A. Lempicki, Systematic and integrative analysis of large gene lists using DAVID bioinformatics resources. *Nat. Protoc.* **4**, 44–57 (2009).
87. D. W. Huang, B. T. Sherman, R. A. Lempicki, Bioinformatics enrichment tools: Paths toward the comprehensive functional analysis of large gene lists. *Nucleic Acids Res.* **37**, 1–13 (2009).
88. B. Gel, A. Díez-Villanueva, E. Serra, M. Buschbeck, M. A. Peinado, R. Malinverni, RegioneR: An R/Bioconductor package for the association analysis of genomic regions based on permutation tests. *Bioinformatics* **32**, 289–291 (2016).

# Acknowledgments

**Funding:** This work was supported by the Ministry of Economy, Industry, and Competitiveness (CGL2014-54317-P and CGL2017-83802-P to A.R.-H.), the Spanish Ministry of Science and Innovation (PID2020-112557GB-I00 founded by AEI/10.13039/501100011033 to A.R.-H.), the Agència de Gestió d'Ajuts Universitaris i de Recerca, AGAUR (2021SGR00122 to A.R.-H.) and the Catalan Institution for Research and Advanced Studies (ICREA Academia to A.R.-H.). L.M.-G. was supported by an FPU predoctoral fellowship from the Ministry of Science, Innovation and University (FPU18/03867). C.V. and L.Á.-G. were supported by FPI predoctoral fellowships from the Ministry of Economy and Competitiveness (BES-2015-072924 and PRE-2018-083257, respectively). A.M.P. was funded by the Ministerio de Ciencia e Innovación (PID2023-152857NB-I00) and Junta de Castilla y León (Unidad de Investigación Consolidada 066, CSI148P20 and CSI017P23). M.A.M.-R. acknowledges support from the Spanish Ministry of Science and Innovation (PID2020-115696RB-I00 and PID2023-151484NB-I00) and the Agència de Gestió d'Ajuts Universitaris i de Recerca, AGAUR (2021SGR01127). **Author contributions:** Conceptualization: A.M.P. and A.R.-H. Methodology: L.M.-G., C.V., R.S.-U., Y.C., N.F.-M., F.G., E.L., A.M.P. and A.R.-H. Investigation: L.M.-G., C.V., R.S.-U., Y.C., N.F.-M., F.G., E.L., M.A.M.-R., A.M.P. and A.R.-H. Visualization: L.M.-G., A.M.P. and A.R.-H. Formal analysis: L.M.-G., L.A.-G., C.V., N.F.-M., M.A.M.-R. and A.R.-H.; Software: L.M.-G. and L.A.-G.; Data curation: L.M.-G., Y.C. and A.R.-H.; Validation: L.M.-G., Y.C., E.L., A.M.-P. and A.R.-H.; Provided resources: Y.C., E.L., A.M.P., M.A.M.-R. and A.R.-H. Funding acquisition: M.A.M.-R., A.M.P. and A.R.-H.; Project administration: A.M.P. and A.R.-H.; Supervision: M.A.M.-R., A.M.P. and A.R.-H. Writing—original draft: L.M.-G. and A.R.-H. Writing—review and editing: L.M.-G., Y.C., E.L., M.A.M.-R., A.M.P. and A.R.-H. **Competing interests:** The authors declare that they have no competing interests. **Data and materials availability:** All data needed to evaluate the conclusions in the paper are present in the paper and/or the Supplementary Materials. Raw data from all the Hi-C experiments performed on this paper on KO fibroblasts, spermatogonia, and primary spermatocytes are available under the NCBI GEO accession number GSE297600. Raw data from the single-cell RNA-seq experiments performed on this paper are available under the NCBI GEO accession number GSE297601. The Hi-C from WT fibroblasts, spermatogonia, and primary spermatocytes, ChIP-seq datasets for REC8, RAD21L, and CTCF from WT spermatocytes, and bulk RNA-seq datasets for WT spermatogonia, spermatocytes, round spermatids and sperm were retrieved from the NCBI GEO repository: GSE132054. ChIP-seq data for H3K4me3, H3K27me3, and H3K27ac modifications from WT mouse spermatocytes were retrieved from the NCBI GEO repository: GSE49624.

Submitted 11 December 2024

Accepted 29 August 2025

Published 1 October 2025

10.1126/sciadv.adv2283